universität wien

MASTERARBEIT / MASTER'S THESIS

Titel der Masterarbeit / Title of the Master's Thesis

„Brownian dynamics simulations of driven deformable cells in ordered polymer networks“

verfasst von / submitted by

Jan Timo Bachmann BSc

angestrebter akademischer Grad / in partial fulfilment of the requirements for the degree of

Master of Science (MSc)

Wien, 2022 / Vienna, 2022

Studienkennzahl lt. Studienblatt / degree programme code as it appears on the student record sheet:	A 066 876
Studienrichtung lt. Studienblatt / degree programme as it appears on the student record sheet:	Masterstudium Physik UG2002
Betreut von / Supervisor:	Univ.-Prof. Dipl.-Ing. Dr. Christos N. Likos
Mitbetreut von / Co-Supervisor:	DI Dr. Andreas Zöttl

Abstract

Various cell types migrate in different environments and in response to different stimuli. Cell migration may include the navigation and locomotion through complex environments, as in the case of Leukocyte migration where cells have to translocate through small pores in the extracellular matrix (ECM) by squeezing their cell body considerably [1].
The aim of this project was to study the influence of pores in the ECM on the speed and surface deformation of cells, using a simplified model of an externally driven deformable cell moving through ordered polymer networks.
The cell and network were modelled as structures of discrete particles interacting via several interaction potentials under the influence of thermal noise. An external force was applied to investigate the propagation of driven deformable cells in networks by means of Brownian dynamics simulations.
A rigid polymer network was chosen as a first simplified model for pores in the ECM. The resulting speed of the driven cell showed oscillatory behaviour with minima before and maxima after each network pore. The speed maxima exceeded the terminal velocity of the respective cell in a network-free fluid, with the speed enhancement being correlated to the total cell interaction energy at the speed maximum. This indicates that in the squeezing process elastic interaction energy is utilized to locally enhance the cell speed. Furthermore, the mean cell speed through the network shows a non-linear unimodal dependence on the bending elasticity of the cell surface bending potential. This unimodal behaviour is mirrored by the maximum cell surface bending energy, implying a causal relationship between both properties.
Finally, simulations using a deformable network were performed successfully, showing oscillatory behaviour in both cell and network properties which represents the bi-directional mechanical crosstalk of cell and network.

Acknowledgements

First, I would like to give thanks to my supervisors. I would like to thank Prof. Christos Likos for his intriguing lectures which inspired me to pursue a Master thesis in this field and his guidance in finding a suitable project. Furthermore, I would like to thank Andreas Zöttl for enabling me to combine my interests in Physics and Biology with his proposed topic. I am thankful for his continuous support during the work on the project, for helping and motivating me along the way and for many fruitful discussions.
A special thanks to my wife and best friend, Julia, for always having my back and enabling me to put so much work in this project.
Finally, I am very grateful for my family, especially my parents, for their unconditional support and for building the basis for all my past and future, personal and professional opportunities.

Contents

List of Figures

List of Tables

Chapter 1

Introduction

Cell migration, referring to the translation of cells from one place to another, plays a crucial role in the development and maintenance of the human body and multicellular organisms in general. This may include the navigation and propagation through complex environments. An example are Leukocytes (white blood cells), which during migration encounter various different surroundings, including environments where they need to translocate through small pores by squeezing their cell body considerably [1]. Depending on the environment and context, cells can migrate along narrow linear structures (1D migration), along sheet-like structures (2D migration), or in a complex three-dimensional environment (3D migration). While many experimental studies have investigated the detailed molecular and biophysical processes involved in 2D migration, much less is currently known about the physical mechanisms of cell migration in complex three-dimensional environments [2].

3D migration shows a variety of different migration modes. However, most of these locomotion strategies share fundamental principles of force generation using the actomyosin cytoskeleton [2], described in the following.
Actin polymerization on the front end of the cell can lead to actin filaments effectively pushing themselves from the front to the back of the cell. Combined with contraction of the cell cortex, this can generate an intracellular rearward-directed force. This force can be coupled by friction to the extracellular environment to produce a net forward motion of the cell. This coupling is often mediated by certain transmembrane adhesion receptors. As a complementary strategy, cortical actomyosin can through contraction generate hydrostatic pressure in order to create so-called blebs, little protrusions which can aid cell propagation.
Exceptions to this force generation method include cells swimming with the aid of helical flagella [3] or cells using the coordinated motion of cilia [4]. Within the discussed cytoskeleton-mediated locomotion framework, the different migratory modes emerge through the varying contributions of adhesion to the extracellular substrate, forward actin protrusion and actomyosin contraction. Two prominent modes are mesenchymal and amoeboid migration [2], visualized in figure 1.1. Mesenchymal migration describes rather elongated cells. Through actin polymerization at the cell front, they generate protrusions and use strong adhesive interactions for locomotion. Amoeboid migration on the other hand makes use of strong cell body deformations while they use only weak adhesive interactions. Environmental factors can also lead to a reversible switching between the two migration modes [2].

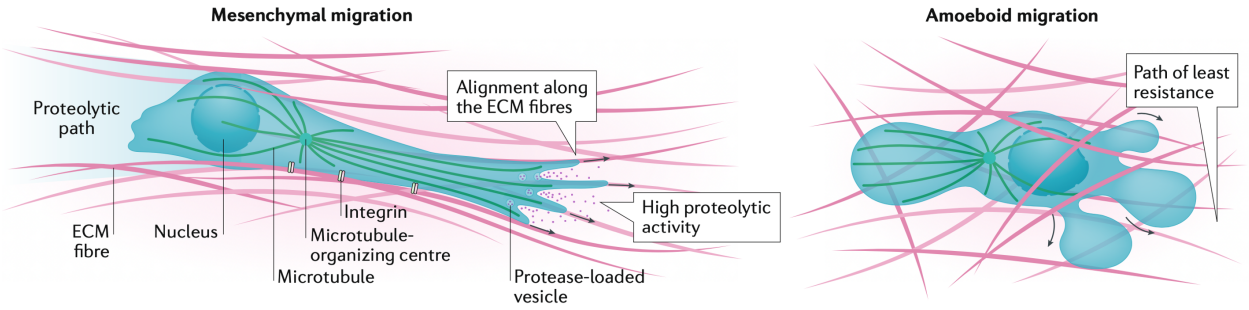

Figure 1.1: Visualization of mesenchymal and amoeboid migration, taken from [2].

Cell migration is an adaptive process. Environmental factors guiding cell adaptations are of chemical, mechanical, and geometrical nature [5]. In general, cells can encounter a broad range of different microenvironments. A prominent example in this case are cancer cells. During the metastatic process, they have to navigate through a variety of different environments [6] like bundled collagen fibres or blood vessels, as visualized in figure 1.2. Cells can penetrate confined environments like small pores using two complementary strategies [7]. They can enlarge the opening through mechanical effects or by degrading parts of the environment. On the other hand, they can deform and change their own shape to squeeze through openings which are significantly smaller than their cell body. This bi-directional relationship between a cell and its environment, which depends on and responds to both physical and chemical stimuli, leads to a coupled evolution of both the cell and the tissue through which it migrates.
A rate-limiting factor of cell body deformations is a cell's nucleus. The nucleus is usually much stiffer than the surrounding cytoplasm. Therefore, once a cell encounters a pore below a critical size, the nucleus becomes a limiting factor resulting in reduced migration speeds [8].

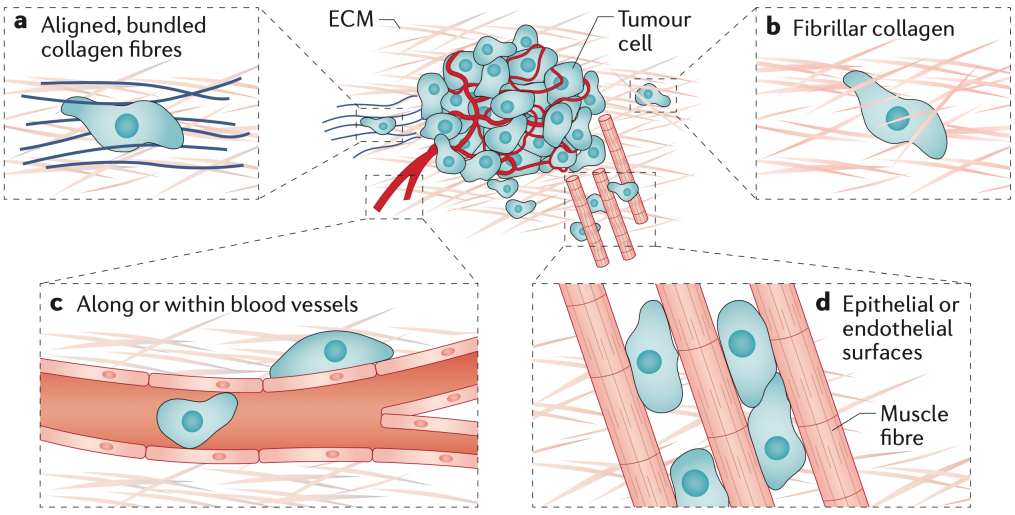

Figure 1.2: Microenvironments for the confined migration of cancer cells, taken from [9].

Cells interact with their environment through their surface which is the cell membrane. Motivated also by the observed variety of shapes of red blood cells (RBC), there have been many efforts to model such membranes in an accurate and realistic manner. The thickness of biological

membranes is several orders of magnitude smaller than the overall size of a typical membrane surface. This motivates the simplified description of the cell surface as a two-dimensional surface embedded in three-dimensional space, which is usually modelled using the triangulation of discrete particles on a surface. Membrane models have been shown to reproduce observed shape transitions when introducing interaction potentials accounting for bending elasticity, shear elasticity as well as geometrical constraints. Examples include investigations of the shape transitions during sedimentation of RBCs [10] or RBCs in capillary flows [11].
The bending potential represents a crucial component in this model. A membrane's bending resistance is typically described by the Helfrich model [12], which describes the bending energy as an integral over the local averaged principle curvatures. The computation of resulting bending forces can be complex, such that studies have been done to investigate the quality of different approaches [13].
Building on this model, computational studies have been done adding surface pattern formation using Reaction-Diffusion equations in order to reproduce amoeboid cell swimming in a pure fluid [14] as well as in a confined environment [15].

This project serves as a first simulation study investigating the mechanical aspects of the aforementioned bi-directional crosstalk during cell migration in confined environments. The influence of pores in the ECM on the speed and surface deformation of cells was investigated using a simplified model of an externally driven deformable cell moving through ordered polymer networks by means of Brownian dynamics simulations.
The simulation methods described in the following chapter introduce the Brownian Dynamics simulation method as well as the relevant interaction potentials which define the cell and network model. The subsequent chapter presents and discusses the results. The conclusion relates the results to the research question and presents an outlook to potential future research.

Chapter 2

Simulation methods

The project's aim was to simulate driven deformable cells in ordered polymer networks. Both cell and network were modelled as structures of discrete particles interacting via several interaction potentials, while their time evolution was investigated using Brownian dynamics simulations. In order to distinguish between cell and network particles, the cell particles are referred to as nodes, while the network particles are referred to as beads in the course of this thesis. Figure 2.1 shows visualizations of the initial configurations of both cell and network, using the software Visual Molecular Dynamics (VMD) [16]. All three-dimensional visualizations in this thesis were created using VMD. The visualization of the cell surface only shows bonds between surface nodes such that the surface is clearly visible. The bonds, however, were drawn automatically in VMD and therefore show additional bonds which are not part of the actual surface triangulation. This applies to all cell surface visualizations in this thesis. The visualization of the network shows the individual network beads, while the sizes of the beads do not necessarily represent the physical bead sizes. The long axis of the network represents the direction in which the cell is pulled.

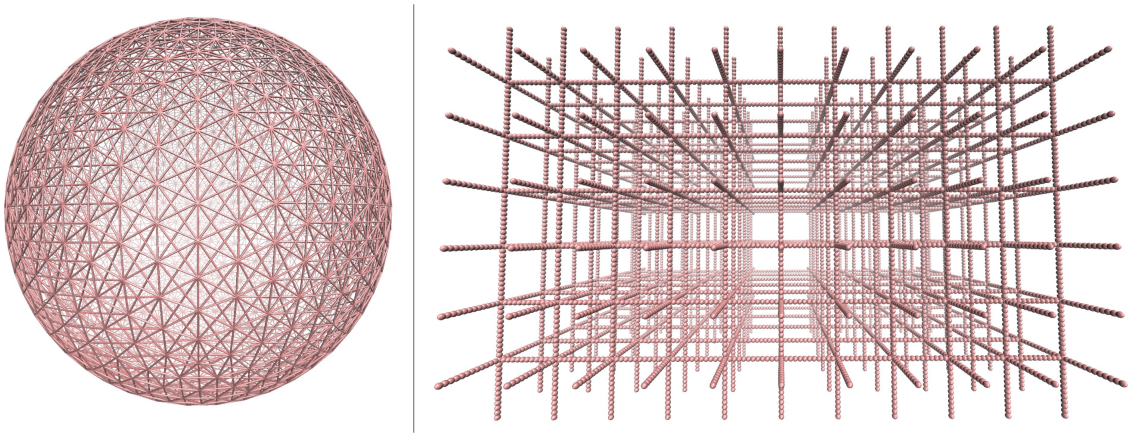

Figure 2.1: Visualization of the initial configurations of both the cell and the network.

Table 2.1 summarizes the simulation methods by presenting the equation of motion governing the particle's time evolution, the implemented integration scheme, as well as the used interaction potentials for the cell and network particles.

Equation of motion:	Brownian dynamics [18] (equation 2.5)
Integration scheme:	Van Gunsteren and Berendsen algorithm [17] (equation 2.8)
Cell interaction potentials:	Bond potential (equation 2.10) Bending potential (equation 2.15) Area potentials (equation 2.16) Volume potential (equation 2.31) SW potentials (equation 2.38)
Network interaction potentials:	WCA potentials (equation 2.48) FENE potentials (equation 2.44) Bending potentials (equation 2.53)
Cell-Network interaction potentials:	WCA potential (equation 2.48)

Table 2.1: Summary of the simulation methods.

2.1 Brownian dynamics

Brownian dynamics is a method used for simulating systems whose behaviour is dominated by thermal fluctuations [18]. Biological systems in the mesoscopic regime are especially suitable for this technique. They fall in the gap between the microscopic atomic-level and the macroscopic continuum-level regime. This mesoscopic approach allows faster simulations, while reproducing the observed diffusion-dominated trajectories. This transition from the microscopic to the mesoscopic regime is visualized in figure 2.2. Instead of simulating individual fluid atoms, the influence of the thermal background is modelled by the sum of a damping force as well as a stochastic force.

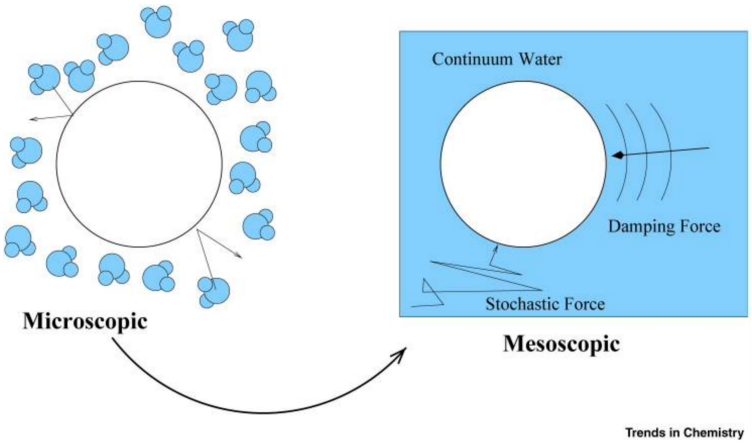

Figure 2.2: Visualization of the mesoscopic approach to simulating dynamics of bodies in a thermal environment, taken from [18].

The starting point for describing the time evolution of a particle in such a system is the Langevin equation for particles of mass m, which is basically Newton's equation of motion with additional terms accounting for friction and stochastic collisions. Considering the one-dimensional time evolution of the position of a particular particle, the Langevin equation reads:

$$m\ddot{x} = -\frac{\mathrm{d}}{\mathrm{d}x}U(x) - \gamma\dot{x} + \sqrt{2\gamma k_B T}\, W(t)\ . \tag{2.1}$$

The dots represent derivatives with respect to time. $U(x)$ represents a potential energy function, γ denotes the friction coefficient, T denotes the fluid temperature. The friction coefficient γ as well as the diffusion constant *D* are asummed to be independent of *x*. $W(t)$ represents a random noise variable satisfying $\langle W(t)\rangle = 0$ and $\langle W(t)W(\tilde{t})\rangle = \delta(t-\tilde{t})$ and is implemented during simulations using a random number generator based on the Ziggurat algorithm [19]. The equation of motion therefore includes force contributions from a potential energy function, a frictional contribution, as well as a stochastic force contribution imitating the effects of thermal collisions with fluid molecules. The impact of the frictional term is stronger for a larger friction coefficient γ, while the impact of the stochastic term is stronger for larger γ or for larger temperature T.
Since a frictional force is present, any initial acceleration resulting from a constant external force will be damped until a constant terminal velocity is reached. A friction force with an additional constant external driving force F_{ext} acting on a particle lead to a terminal velocity which is proportional to the strength of the driving force. The constant of proportionality is the so-called mobility μ. Using the Einstein relation, one can identify the mobility as the ratio of the diffusion constant and the thermal energy $\mu = \frac{D}{k_B T}$. This gives an analytical prediction for the terminal velocity:

$$v_{terminal} = \mu F_{ext} = \frac{D}{k_B T} F_{ext}\ . \tag{2.2}$$

The timescale of the damping of the initial acceleration can be quantified by the relaxation time:

$$\tau \equiv \frac{m}{\gamma}\ . \tag{2.3}$$

For typical cells with sizes in the micrometer range moving in an aqueous environment, this timescale is negligibly small. In this overdamped regime, the left-hand side of the Langevin equation (2.1) is negligible and can be set to zero:

$$0 = -\frac{\mathrm{d}}{\mathrm{d}x}U(x) - \gamma\dot{x} + \sqrt{2\gamma k_B T}\, W(t)\ . \tag{2.4}$$

Using the Einstein relation $\gamma D = k_B T$, this can be rewritten to the one-dimensional Brownian dynamics equation of motion:

$$\dot{x}(t) = -\frac{D}{k_B T}\frac{\mathrm{d}}{\mathrm{d}x}U(x) + \sqrt{2D}\, W(t)\ . \tag{2.5}$$

In order to simulate Brownian dynamics, one needs a discretized version of equation 2.5. For the following considerations, the derivative of the potential with respect to the position is rewritten as the force *F*. The simplest algorithm, the so-called Conventional Brownian Dynamics (CBD) algorithm [17], is at the level of the first-order Euler method for ordinary differential equations, thus requiring a rather small time step to provide satisfying results:

$$\Delta x = \frac{D}{k_B T}F(x,t)\Delta t + \sqrt{2D\Delta t}\, W(t)\ . \tag{2.6}$$

At zero external force, this algorithm reproduces $\langle \Delta x \rangle = 0$ and $\langle \Delta x^2 \rangle = 2D\Delta t$, as expected for diffusive motion. There are higher-order Runge-Kutta-like methods which, however require multiple force evaluations per time step. An alternative algorithm proposed by van Gunsteren and Berendsen (GB) [17] provides an improvement to the CBD algorithm, while only requiring one force evaluation per time step. The GB algorithm replaces the force $F(x,t)$ in equation 2.6 with $\frac{1}{2}[2F(x,t) + \Delta t\dot{F}(x,t)]$ with $\dot{F}(x,t) \equiv \frac{1}{\Delta t}[F(x,t) - F(x,t-\Delta t)]$. This yields:

$$\Delta x = \frac{1}{2}\frac{D}{k_B T}[3F(x,t) - F(x,t-\Delta t)]\Delta t + \sqrt{2D\Delta t}\, W(t)\ . \tag{2.7}$$

This can be extended to a three-dimensional algorithm to update the position coordinates of both cell nodes and network beads. Starting from an initial configuration, the position coordinate *j* ($j \in 1,2,3$) of particle *i* can be updated according to:

$$r_i^j(t+\Delta t) = r_i^j(t) + \frac{D}{2k_B T}[3F_i^j(t) - F_i^j(t-\Delta t)]\Delta t + \sqrt{2D\Delta t}\, W(t)\ . \tag{2.8}$$

Here, the particles $i \in 1,...N$ include both cell nodes N_{nodes} and network beads N_{beads} such that $N = N_{nodes} + N_{beads}$. The force vector on each particle *i* contains the gradient of the sum U_{tot} of all its interaction potentials. The external driving force pulling the cell through the network was simulated by applying a constant force $\vec{F}_{ext}$ on each cell node. Therefore, the force vector on cell node *j* contains the potential forces as well as the external force:

$$\vec{F}_j = -\vec{\nabla}_j U_{tot,j}(\vec{r}_1, ...\vec{r}_{N_{nodes}}) + \vec{F}_{ext} \quad j = 1, ...N_{nodes} \tag{2.9}$$

So, from knowledge of the current forces acting on all particles of the system, one can calculate the positions of all particles at the next time step. In order to calculate the acting forces, one first needs to define all interaction potentials between the different particles of the system. The next chapter describes the simulation methods including the definitions of all relevant interaction potentials used in this project.

2.2 Cell model

Model overview

The thickness of biological membranes is several orders of magnitude smaller than the overall size of a typical membrane surface, which motivates the simplified description of the cell surface as a two-dimensional surface embedded in three-dimensional space. Therefore, the cell nodes are initialized on a spherical surface forming a triangulated surface. Interaction potentials between individual surface nodes were introduced such that the collective surface behaviour reproduces some typical mechanical behaviour of biological cells or vesicles encapsulated by lipid bilayer membranes. The behaviour of the cell surface is influenced not only by the cell membrane, but also its intracellular components like protein filaments of the cytoskeleton. In principle, different

potentials with different strengths could be used to mimic the variability in cell mechanical properties of different cells.

The triangulation of the cell was performed using a so-called Delaunay triangulation. Delaunay triangulation is a popular method in computational geometry [20] . Starting from a set of discrete nodes on a spherical surface, the method allows to produce a grid of triangles connecting the nodes while satisfying the Delaunay condition: the circumcircle of each triangle contains only the nodes of the respective triangle. This way, one has a clean surface spanned by neighbouring triangles, such that the triangle nodes and edges can be later used for force computations accounting for properties like bending rigidity. An example for a Delaunay triangulation is given in figure 2.3a.
The grid resolution of the Delaunay triangulation is quantified by a triangulation factor. For the simulations of this project, a factor of 10 was used. This generates a surface containing 1002 nodes. The topology then restricts the surface to have 3000 edges (bonds) and 2000 faces (triangles). Most of the surface nodes have 6 nearest neighbours, while a few only have 5. A larger factor leads to a smoother surface and thus a better representation of a continuous surface, but also leads to higher computational cost. Using a factor of 10, the surface area and volume deviation of the initialized surface from a perfect sphere is rather small while the computational cost is bearable. Due to the Delaunay triangulation, the individual cell surface bonds follow a bond length distribution instead of having just one single value. The initial bond lengths were normalized by their initial mean value b_0. Figure 2.3b shows a histogram of the initial bond lengths b with a bin size of about 0.01.

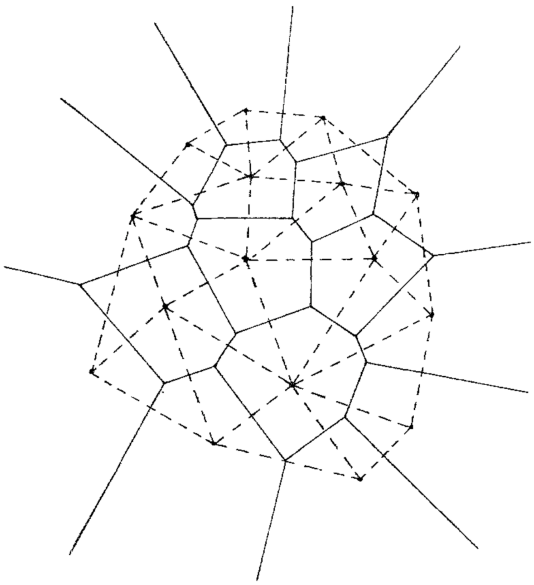

(a) Visualization of a Delaunay triangulation of a discrete set of points, taken from [21]. The dashed lines represent the Delaunay triangulation.

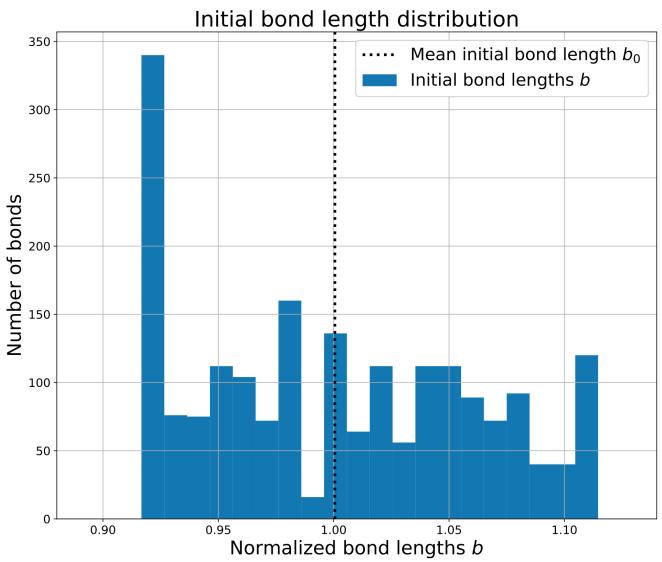

(b) Initial surface bond length distribution of the triangulated cell surface. The individual bond lengths were normalized to their mean value.

Figure 2.3: Delaunay triangulation of the cell surface

The possibility to initialize the cell as an ellipsoid of a given axis ratio was also implemented. Figure 2.4 shows a visualization of an ellipsoidal cell. An ellipsoidal geometry allows the surface

to take different shapes of minimal energy when including a bending potential and constraints of constant volume and area. In the case of a sphere, the constraints would allow only small deformations. However, simulations using ellipsoidal initial cells were not performed in the course of this project.

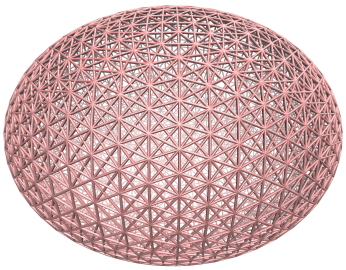

Figure 2.4: Visualization of an ellipsoidal cell, initialized with axis ratios 1:1:1.3.

Interaction potentials accounting for elasticity, bending rigidity as well as the tendency to keep a constant surface area and volume were implemented. In order to account for those interactions in a simulation, one has to derive analytical expressions for the resulting force contributions, such that those can be computed using only knowledge of the position coordinates of all participating particles. In the following, the implemented interaction potentials are described and the necessary force expressions are derived. All force expressions were derived as part of this project, except the bending forces of both cell surface and network chains.

Bond potential

A harmonic bond potential was used for the edges (bonds) of the triangulated surface, such that deviations from the respective equilibrium bond length cost energy. The strength of the interaction is given by k_{Bend}, while the equilibrium bond length is $r_{ij,0}$. Let $\vec{r}_{ij} \equiv \vec{r}_i - \vec{r}_j$ be the bond vector connecting nodes *i* and *j*, with length $r_{ij} \equiv |\vec{r}_{ij}|$. The unit distance vector is defined as $\hat{\vec{r}}_{ij} \equiv \frac{\vec{r}_{ij}}{r_{ij}}$. Let *B* be the set of surface bonds. The total bond potential is then given by:

$$U_{Bond} = \frac{k_{Bond}}{2} \sum_{ij \in B} (r_{ij} - r_{ij,0})^2 \ . \tag{2.10}$$

The gradient with respect to the position of node *i*, $\vec{\nabla}_i \equiv (\frac{\partial}{\partial x_i}, \frac{\partial}{\partial y_i}, \frac{\partial}{\partial z_i})^T$, of the bond vector can be written as:

$$\vec{\nabla}_i r_{ij} = \vec{\nabla}_i \, |\vec{r}_i - \vec{r}_j| = \frac{\vec{r}_i - \vec{r}_j}{|\vec{r}_i - \vec{r}_j|} = \frac{\vec{r}_{ij}}{r_{ij}} = \hat{\vec{r}}_{ij} \ . \tag{2.11}$$

Let B_i be the set of bonds node *i* contributes to. The resulting force on membrane node *i* with position $\vec{r}_i$ can therefore be obtained by:

$$\vec{F}_{Bond,i} = -\vec{\nabla}_i U_{Bond} = -k_{Bond} \sum_{j \in B_i} [\ (r_{ij} - r_{ij,0})\ \vec{\nabla}_i r_{ij}\ ] = -k_{Bond} \sum_{j \in B_i} [\ (r_{ij} - r_{ij,0})\, \hat{\vec{r}}_{ij}\ ] \ . \tag{2.12}$$

The resulting bond force on node *i* can therefore be written as:

$$\vec{F}_{Bond,i} = -k_{Bond} \sum_{j \in B_i} [\ (r_{ij} - r_{ij,0})\, \hat{\vec{r}}_{ij}\ ]\ . \tag{2.13}$$

For $r_{ij} < r_{ij,0}$ this will result in a force pushing node *i* further away from *j*, while $r_{ij} > r_{ij,0}$ results in a force pulling node *i* towards *j*.

Bending potential for a membrane surface

According to the Helfrich model [12], the curvature energy of the triangulated surface can be computed as a quantity proportional to the integrated local mean curvature. The local mean surface curvature is defined as the average of the inverse principle radii of curvature $H = \frac{1}{2}[\frac{1}{R_1} + \frac{1}{R_2}]$. The total surface curvature energy can then be computed using the bending modulus k_{Bend}:

$$U = 2k_{Bend} \int_S [H(\vec{r}) dS(\vec{r})]\ . \tag{2.14}$$

S denotes the continuous membrane surface. The minimum energy configuration would in this case be zero curvature and thus a flat sheet. A reference curvature representing a different minimum energy configuration could in principle be included in the curvature energy. It should also be noted that the actual curvature energy has another energy contribution which, however, is constant for constant topology. Since the curvature energy is mainly used for force calculations in this project, this additional contribution cancels and can be dropped in this context [12]. When simulating such a membrane, one deals with discrete particles approximately representing a continuous surface. Guckenberger et al. [13] describe and compare different algorithms to compute bending forces for triangulated surfaces. The method used in this project is described as method B in [13] and computes the curvature energy using a discretized version of the Laplace-Beltrami operator Δ_S. The Laplace-Beltrami operator represents a generalization of the Laplace operator defined on submanifolds in Euclidian space. The resulting force expression for a discretized triangulated surface is a large expression with several different contributions. The exact form can be found in [13]. The essential point is that one ends up with an analytical expression to compute the resulting bending force on node *i* from knowledge of the positions of all membrane nodes:

$$\vec{F}_{Bend,i} = [-\vec{\nabla}_i U_{Bend}]\ (\vec{r}_1, ...\vec{r}_i, ...\vec{r}_N)\ . \tag{2.15}$$

This interaction was implemented to act on all surface nodes.

Area potential

A harmonic potential was used to simulate the tendency of keeping a constant area. Individual potentials were implemented to act locally on each surface triangle. The interaction strength is given by k_A, while the respective equilibrium area of triangle *t* is given by A_t. Let *T* be the set of all surface triangles, then the total surface area is given by $A_{tot} = \sum_{t \in T} A_t$. The total potential can then be written as:

$$U_A = \frac{k_A}{2} \sum_{t \in T} (A_t - A_{t,0})^2. \tag{2.16}$$

Let T_i be the set of triangles which node *i* contributes to. The resulting force on membrane node *i* can then be calculated as:

$$\vec{F}_{A,i} = -\vec{\nabla}_i U_A = -k_A \sum_{t \in T_i} [\ (A_t - A_{t,0})\ \vec{\nabla}_i A_t\ ]\ . \tag{2.17}$$

For the following derivation, a particular triangle $t \in T_i$ is considered and denoted by A. This allows to calculate a single contribution to the force on node *i*, such that afterwards all single contributions can be summed up to obtain the total force on node *i*. In order to determine the force vector, one needs analytical expressions for the surface area as well as its gradient. Let the three nodes constituting the triangle A be *i*, *j*, and *k*. The surface area can then be obtained by :

$$A = \frac{1}{2} |(\vec{r_i} - \vec{r_j}) \times (\vec{r_i} - \vec{r_k})|\ . \tag{2.18}$$

For the following calculations, the notation is further being uncluttered by rewriting $a \equiv \vec{r_i}$, $b \equiv \vec{r_j}$, and $c \equiv \vec{r_k}$. The task then translates to calculating $\vec{\nabla}_a A$ with $A = \frac{1}{2}|(a-b) \times (a-c)|$. Identifying the absolute value of a vector with the square root of the scalar product of the vector with itself, as well as using the chain rule, one finds:

$$\vec{\nabla}_a A = \frac{1}{4} \frac{1}{|(a-b) \times (a-c)|}\ \vec{\nabla}_a [\ [(a-b) \times (a-c)] \cdot [(a-b) \times (a-c)]\ ]. \tag{2.19}$$

In order to calculate the gradient term on the right hand side, the Levi-Civita tensor ϵ_{ijk} and the Kronecker delta δ_{ij} are used, both defined in the following, as well as Einstein's summation convention:

$$\epsilon_{ijk} = \begin{cases} +1 & \text{for even permutations of i,j,k} \\ -1 & \text{for uneven permutations of i,j,k} \\ 0 & \text{else} \end{cases} \qquad \delta_{lm} = \begin{cases} +1 & \text{for } \ l = m \\ 0 & \text{for } \ l \neq m\ . \end{cases} \tag{2.20}$$

The gradient term on the right hand side of equation (2.19) can thus be written component-wise as:

$$\nabla_{a_i}\ [\ \epsilon_{jkl}(a-b)_k (a-c)l\ \epsilon_{jmn}(a-b)_m (a-c)_n\ ] \tag{2.21}$$

which, using the product rule, yields:

$$[\nabla_{a_i} \epsilon_{jkl}(a-b)_k (a-c)_l]\ \epsilon_{jmn}(a-b)_m (a-c)_n\ +\ \epsilon_{jkl}(a-b)_k (a-c)_l\ [\nabla_{a_i} \epsilon_{jmn}(a-b)_m (a-c)_n] \tag{2.22}$$

Using $\nabla_{a_i} a_k = \delta_{ik}$, this gives:

$$\begin{aligned} \nabla_{a_i} \epsilon_{jkl}(a-b)_k (a-c)_l &= \epsilon_{jkl}\ [\ (a-b)_k\ \nabla_{a_i}(a-c)_l\ +\ (a-c)_l\ \nabla_{a_i}(a-b)_k\ ] \\ &= \epsilon_{jkl}\ [\ (a-b)_k\ \delta_{il}\ +\ (a-c)_l\ \delta_{ik}\ ]. \end{aligned} \tag{2.23}$$

One can then use the identity $\epsilon_{jkl}\epsilon_{jmn} = \delta_{km}\delta_{ln} - \delta_{kn}\delta_{lm}$ to rewrite the left-hand term of the sum in equation 2.22 as:

$$\begin{aligned} \epsilon_{jkl}\epsilon_{jmn}\ [\ (a-b)_k\ \delta_{il}\ +\ (a-c)_l\ \delta_{ik}\ ]\ [\ (a-b)_m (a-c)_n\ ] \\ = [\ \delta_{km}\delta_{ln} - \delta_{kn}\delta_{lm}\ ]\ [\ (a-b)_k\ \delta_{il}\ +\ (a-c)_l\ \delta_{ik}\ ]\ [\ (a-b)_m (a-c)_n\ ] \end{aligned} \tag{2.24}$$

Using $\delta_{km}\delta_{ik} = \delta_{im}$, this reduces to:

$$\begin{aligned}
&[\ \delta_{im}(a-c)_n - \delta_{in}(a-c)_m + \delta_{in}(a-b)_m - \delta_{im}(a-b)_n\ ]\ [\ (a-b)_m(a-c)_n\ ] \\
&\qquad = [\ \delta_{im}(b-c)_n - \delta_{in}(c-b)_m\ ]\ [\ (a-b)_m(a-c)_n\ ] \\
&\qquad = (a-b)_i(b-c)_n(a-c)_n + (a-c)_i(c-b)_m(a-b)_m \\
&\qquad = (a-b)_i\ [\ (b-c)\cdot(a-c)\ ]\ +\ (a-c)_i\ [\ (c-b)\cdot(a-b)\ ]. \quad (2.25)
\end{aligned}$$

The above term is equal to the left-hand part of the sum in equation (2.22). The right hand side term in the sum is equal to the left, only with change of indices $(k,l) \mapsto (m,n)$. Since those indices do not appear in the resulting expression, one can conclude that the right hand side term has the exact same contribution to the gradient.
This gives the gradient term which can be inserted into equation (2.19) to obtain an expression for $\vec{\nabla}_a A$:

$$\vec{\nabla}_a A = \frac{2\ [\ (a-b)\ [(b-c)\cdot(a-c)]\ +\ (a-c)\ [(c-b)\cdot(a-b)]\ ]}{4\ |(a-b)\times(a-c)|}. \quad (2.26)$$

In order to reduce the number of operations needed to perform the calculation of one gradient, one can simplify the above equation using the Graßmann identity: $\vec{a}\times(\vec{b}\times\vec{c}) = (\vec{a}\cdot\vec{c})\,\vec{b} - (\vec{a}\cdot\vec{b})\,\vec{c}$. Therefore:

$$(a-b)\ [(b-c)\cdot(a-c)]\ +\ (a-c)\ [(c-b)\cdot(a-b)]\ =\ (b-c)\times[(a-b)\times(a-c)] \quad (2.27)$$

Inserting this result into the area gradient term and changing back to the original notation for the position vectors leads to :

$$\vec{\nabla}_i A = \frac{2\ (\vec{r}_j-\vec{r}_k)\times[(\vec{r}_i-\vec{r}_j)\times(\vec{r}_i-\vec{r}_k)]}{4\ |(\vec{r}_i-\vec{r}_j)\times(\vec{r}_i-\vec{r}_k)|} = \frac{(\vec{r}_j-\vec{r}_k)\times\vec{A}}{2A} \quad (2.28)$$

with $\vec{A} = \frac{1}{2}[(\vec{r}_i-\vec{r}_j)\times(\vec{r}_i-\vec{r}_k)]$ and $A = |\vec{A}|$.
The expression for the area gradient can be inserted into equation (2.17) to obtain an expression for the single contribution to the area force on node *i*:

$$\vec{F}_{A,i} = -\frac{k_A}{2}\ (A-A_0)\ \frac{(\vec{r}_j-\vec{r}_k)\times\vec{A}}{2A} = \frac{k_A}{4}\ [\frac{A_0}{A}-1]\ [(\vec{r}_j-\vec{r}_k)\times\vec{A}]\ . \quad (2.29)$$

Let j_t and k_t be the nodes which together with node *i* constitute triangle $t \in T_i$ and let A_t be defined according to equation 2.18. The contributions of all participating triangles can then be summed up to obtain an expression for the resulting area force on node *i*:

$$\vec{F}_{A,i} = \frac{k_A}{4}\ \sum_{t\in T_i}\ [\frac{A_{t,0}}{A_t}-1]\ [(\vec{r}_{j_t}-\vec{r}_{k_t})\times\vec{A}_t] \quad (2.30)$$

The effect of an area deviation on the resulting area force can be checked by considering an equilateral triangle in the xy-plane, centered at the origin, with r_i pointing in positive x-direction. The force contribution of A_t on this node *i* is considered. The vector $(r_j - r_k)$ then points in y-direction and the area vector stands normal on the triangle, in this case pointing in positive z-direction. Therefore, their cross product points in positive x-direction, which is also the direction in which the force would act. Now, if $A_t < A_{t,0}$, the prefactor will be larger than zero such that a

force will push r_1 to larger x-values, resulting in a triangle area increase. If $A_t > A_{t,0}$, the prefactor will be smaller than zero such that a force will pull r_1 to smaller x-values, resulting in a triangle area decrease. Equation (2.30) also shows that there is only a force contribution from triangle *t* for $A_t \neq A_{t,0}$. This is exactly what one would expect from the chosen potential in equation (2.30).

Alternatively to the chosen potential (2.16) one could define one single area potential acting on the cell as a whole, such that deviations of the total surface area from the equilibrium total surface area cost energy. This would lead to a similar expression as equation (2.30). However, the prefactor would change from an individual triangle prefactor to one global prefactor for all individual triangle contributions. As in this case local perturbations would be fought globally instead of locally, this could lead to a more unstable configuration.

Volume potential

Another harmonic potential was used to simulate the tendency of keeping a constant volume. The interaction strength is given by k_V, while the equilibrium total volume is given by V_0. The potential thus reads:

$$U_V = \frac{k_V}{2}(V - V_0)^2. \tag{2.31}$$

In order to calculate the force, the total volume is separated into individual volume contributions. Each surface triangle contributes a tetrahedral volume element to the total volume. Let T_i be the set of all surface triangles. The total volume is then given by $V = \sum_{t \in T_i} V_t$. Using $\vec{\nabla}_i V = \sum_t \vec{\nabla}_i V_t$, the total force on node *i* can thus be splitted into contributions from each surface triangle *t*:

$$\vec{F}_{V,i} = -\vec{\nabla}_i U_V = -k_V(V - V_0)\vec{\nabla}_i V = \sum_t (-k_V)\ (V - V_0)\ \vec{\nabla}_i V_t \ \equiv \ \sum_t \vec{F}_{V_t,i}\ . \tag{2.32}$$

In the following, the force contribution $\vec{F}_{V_t,i} = -k_V(V - V_0)\vec{\nabla}_i V_t$ of volume element V_t is considered. The tetrahedral volume element is built by connecting the three nodes of the corresponding surface triangle with the center of mass of the membrane. The positions of the three surface triangle nodes are again called $\vec{r_i}, vecr_j, vecr_k$. They are connected to the membrane's center of mass $vecr_c$. This gives a tetrahedron for which the volume can be calculated using the triple product:

$$V_t = \frac{1}{6}\ |\ (\vec{r_i} - \vec{r_c}) \cdot [\ (\vec{r_j} - \vec{r_c}) \times (\vec{r_k} - \vec{r_c})\ ]\ | \tag{2.33}$$

There is some freedom in choosing which tetrahedron edges to use at which part in the triple product. However, when having to calculate the gradient with respect to $\vec{r_i}$, the above choice

makes the computation easier:

$$\begin{aligned}\vec{\nabla}_i \tilde{V} &= \frac{1}{6}\vec{\nabla}_i \sqrt{[\ (\vec{r_i}-\vec{r_c})\cdot[\ (\vec{r_j}-\vec{r_c})\times(\vec{r_k}-\vec{r_c})\ ]\ ]^{\,2}} \\ &= \frac{1}{6}\frac{(\vec{r_i}-\vec{r_c})\cdot[\ (\vec{r_j}-\vec{r_c})\times(\vec{r_k}-\vec{r_c})\ ]}{|\ (\vec{r_i}-\vec{r_c})\ [\ (\vec{r_j}-\vec{r_c})\times(\vec{r_k}-\vec{r_c})\ ]\ |}\ \vec{\nabla}_i[\ (\vec{r_1}-\vec{r_c})\cdot[(\vec{r_j}-\vec{r_c})\times(\vec{r_k}-\vec{r_c})]\ ] \\ &= \frac{1}{6}\frac{(\vec{r_i}-\vec{r_c})\cdot[\ (\vec{r_j}-\vec{r_c})\times(\vec{r_k}-\vec{r_c})\ ]}{|\ (\vec{r_i}-\vec{r_c})\cdot[\ (\vec{r_j}-\vec{r_c})\times(\vec{r_k}-\vec{r_c})\ ]\ |}\ [(\vec{r_j}-\vec{r_c})\times(\vec{r_k}-\vec{r_c})] \quad (2.34)\end{aligned}$$

The quotient term only contributes a sign ± 1, depending on the angle between the vectors $(\vec{r_i}-\vec{r_c})$ and $(\vec{r_j}-\vec{r_c})\times(\vec{r_k}-\vec{r_c})$. The vector of the cross product stands orthogonal on the area spanned by the two vectors of the cross product. Assuming the indices are counted counterclockwise, it points in a similar direction as $\vec{r_1}$ (but with a non-zero angle to $\vec{r_1}$). The angle between those vectors will always be between 0°and 90°. Therefore, their scalar product is larger than zero, and the quotient of the scalar product and its absolute value will be $+1$, such that:

$$\vec{\nabla}_i V_t = \frac{1}{6}[(\vec{r_j}-\vec{r_c})\times(\vec{r_k}-\vec{r_c})]\ . \quad (2.35)$$

Therefore :

$$\vec{F}_{V_t,i} = -k_V\ (V-V_0)\ \frac{1}{6}[\ (\vec{r_j}-\vec{r_c})\times(\vec{r_k}-\vec{r_c})\ ]\ . \quad (2.36)$$

Let j_t and k_t be the nodes which together with node *i* constitute triangle $t \in T_i$. The resulting force contribution on node *i* can then be written as:

$$\vec{F}_{V,i} = \frac{k_V}{6}(V_0-V)\sum_{t\in T_i}[\ (\vec{r_{j_t}}-\vec{r_c})\times(\vec{r_{k_t}}-\vec{r_c})\ ]\ . \quad (2.37)$$

The cross product in the force contribution points orthogonal to both vectors of the product, roughly in the direction of $\vec{r_i}$. Therefore, for $V < V_0$ there will be a force pushing node *i* away from the center of the triangle, leading to a surface area and thus volume increase. The reverse holds for $V > V_0$.

Stillinger-Weber potential

In order to prevent surface bonds from potentially rupturing, an additional Stillinger-Weber (SW) potentials was implemented to optionally act on all surface bonds, as an addition to the harmonic bond interactions. This is based on the description in [10]. The additional potential consists of an attractive as well an repulsive contribution. The idea is that the interaction generates a strong force pulling the bonds back towards equilibrium length once the displacement is sufficiently large.
A particular surface bond with bond vector $\vec{r_{ij}}$ is considered in the following. The attractive potential for a bond vector $\vec{r_{ij}}$ reads:

$$U_{SW,A} = \begin{cases} \frac{k_{SW}}{l_{max}-r_{ij}} \exp\left\{\frac{1}{l_{c,0}-r_{ij}}\right\} & \text{for } r_{ij} > l_{c,0} \\ 0 & \text{else} \end{cases} \tag{2.38}$$

Assuming $r > l_{c,0}$, this gives a force contribution according to:

$$\begin{aligned} \vec{F}_{SW,A,i} &= -\vec{\nabla}_i U_{SW,A} \\ &= -k_{SW} \left[\left(\vec{\nabla}_i \exp\left\{\frac{1}{l_{c,0}-r_{ij}}\right\}\right) \frac{1}{l_{max}-r_{ij}} + \exp\left\{\frac{1}{l_{c,0}-r_{ij}}\right\} \left(\vec{\nabla}_i \frac{1}{l_{max}-r_{ij}}\right) \right] \vec{\nabla}_i r \\ &= -\frac{k_{SW}}{l_{max}-r_{ij}} \exp\left\{\frac{1}{l_{c,0}-r_{ij}}\right\} \left[\frac{1}{(l_{c,0}-r_{ij})^2} + \frac{1}{l_{max}-r_{ij}}\right] \vec{\nabla}_i r_{ij} \end{aligned} \tag{2.39}$$

The resulting attractive force contribution can thus be expressed as:

$$\vec{F}_{SW,A,i} = \left[-\frac{k_{SW}}{l_{max}-r_{ij}} \exp\left\{\frac{1}{l_{c,0}-r_{ij}}\right\} \left[\frac{1}{(l_{c,0}-r_{ij})^2} + \frac{1}{l_{max}-r_{ij}}\right] \right] \frac{\vec{r}_{ij}}{r_{ij}} \,. \tag{2.40}$$

So, for some $l_{c,0} < r_{ij} < l_{max}$, all individual terms in the brackets in the above force expression are positive, such that, taking into account the negative sign at the front, the force really does act as an attractive force.
The repulsive potential reads:

$$U_{SW,R} = \begin{cases} \frac{k_{SW}}{r_{ij}-l_{min}} \exp\left\{\frac{1}{r_{ij}-l_{c,1}}\right\} & \text{for } r_{ij} < l_{c,1} \\ 0 & \text{else} \end{cases} \tag{2.41}$$

Again, the resulting force contribution is computed:

$$\begin{aligned} \vec{F}_{SW,R,i} &= -\vec{\nabla}_i U_{SW,R} \\ &= -k_{SW} \left[\left(\vec{\nabla}_i \exp\left\{\frac{1}{r_{ij}-l_{min}}\right\}\right) \frac{1}{r_{ij}-l_{min}} + \exp\left\{\frac{1}{r_{ij}-l_{c,1}}\right\} \left(\vec{\nabla}_i \frac{1}{r_{ij}-l_{min}}\right) \right] \vec{\nabla}_i r_{ij} \\ &= -\frac{k_{SW}}{r_{ij}-l_{min}} \exp\left\{\frac{1}{r_{ij}-l_{c,1}}\right\} \left[-\frac{1}{(r_{ij}-l_{c,1})^2} - \frac{1}{r_{ij}-l_{min}}\right] \vec{\nabla}_i r_{ij} \end{aligned} \tag{2.42}$$

The resulting repulsive force contribution can thus be expressed as:

$$\vec{F}_{SW,R,i} = \left[\frac{k_{SW}}{r_{ij}-l_{min}} \exp\left\{\frac{1}{r_{ij}-l_{c,1}}\right\} \left[\frac{1}{(r_{ij}-l_{c,1})^2} + \frac{1}{r_{ij}-l_{min}}\right] \right] \frac{\vec{r}_{ij}}{r_{ij}} \tag{2.43}$$

So, for some $l_{min} < r_{ij} < l_{c,1}$, all individual terms in the brackets in the above force expression are positive, such that the force really does act as a repulsive force.

Furthermore, it holds that $l_{min} < l_{c,1} < l_{c,0} < l_{max}$. The bond length is then effectively restricted to the range $l_{min} < r < l_{max}$, while in the range $l_{c,1} < r < l_{c,0}$ the resulting SW force is zero. For a proper choice of parameters, this gives a good way to prevent bond rupturing, since parameters can be chosen such that under normal conditions there is no additional force contribution. But if bond length displacements are sufficiently large, the SW interaction contributes a strong force, effectively restricting the bond lengths to a desired range.

The top plot in figure 2.5 shows the combined SW potential using $k_{SW} = 10$, $l_{min} = 0.67$, $l_{c,1} = 0.85$, $l_{c,0} = 1.15$, and $l_{max} = 1.33$, inspired by the choice of parameter values in [10], as well as the individual contributions from the attractive ($U_{SW,A}$) and repulsive ($U_{SW,R}$) part. The bottom plot shows the impact of a SW potential as an addition to a harmonic bond potential with $k_{Bond} = 10^2$ and $x_0 = 1$. For small bond distance displacements, the SW potential has no impact. As the distance approaches l_{min} or l_{max}, the SW potential contributes a strong potential gradient, leading to a strong force trying to restore the equilibrium distance.

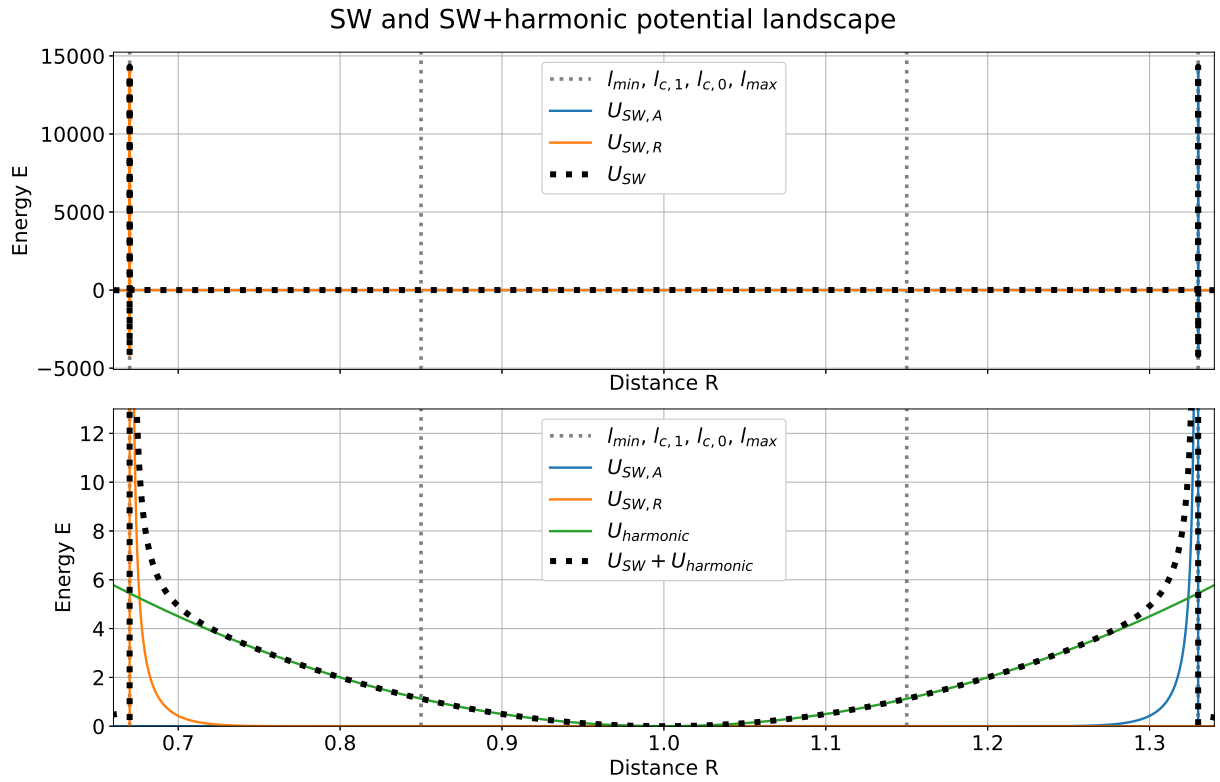

Figure 2.5: Visualization of the energy landscapes of SW and SW+Bond potentials. The chosen parameters were $k_{SW} = 10$, $l_{min} = 0.67$, $l_{c,1} = 0.85$, $l_{c,0} = 1.15$, $l_{max} = 1.33$, $k_{Bond} = 10^2$ and $x_0 = 1$.

2.3 Network model

Model overview

The cell's environment is modeled as an ordered polymer network. A rectangular cuboid is chosen as the system's box with two equally long axes (x and y) and one larger axis (z). The larger axis is chosen to be the direction of the acting driving force. The network can be viewed as being built of individual cubes or unit cells, such that the number of unit cells $N_{cells,z}$ along the z-direction determines the length and the number of unit cells $N_{cells,xy}$ along the x- and y-direction determines the size of the network. In the x- and y-direction, additional polymer strands attach the outer network cells to the walls of the simulation box, as seen in figure 2.1. The individual chains consist of identical polymer beads at close contact. Beads are crosslinked when three chains meet, at the corners of each unit cell, those are therefore part of all three chains including their interactions.
The implemented algorithm constructs such a network based on the variable input of four characteristic length quantities: the polymer bead diameter d, the network grid size a_{grid}, as well as the number of cells in both x/y- and z-direction: $N_{cells,xy}$ and $N_{cells,z}$.
The interactions between the polymer beads are based on the Kremer-Grest model [23] for polymer chains. The bonds between neighbouring beads within a chain are simulated by an attractive and a repulsive potential contribution. The repulsive contributions are modeled by Weeks-Chandler-Andersen (WCA) [24] potentials while the attractive contributions are modeled by Finitely Extensible Nonlinear Elastic (FENE) bond potentials. An additional contribution accounting for the bending of a polymer chain is given using a potential for angular displacements. The interactions between membrane nodes of the cell and polymer beads of the network are modeled by purely repulsive WCA potentials.

Network construction

From the input parameters, all other necessary characteristic network parameters can be computed:

- The number of beads which construct one edge of a unit cell: $N_{dpa} = \frac{a_{grid}}{d} + 1$.
- The number of crosslinks in both directions: $N_{c,xy} = N_{cells,xy} + 1$ and $N_{c,z} = N_{cells,z} + 1$.
- The number of beads on each chain in both directions: $N_{xy} = (N_{c,xy} + 1)a_{grid} + 1$ and $N_z = (N_{c,z} - 1)a_{grid} + 1$.
- The rectangular cubic box dimensions: $L_{xy} = (N_{xy} - 1)d$ and $L_z = (N_z - 1)d + 2a_{grid}$.

The network is built in two steps. First, the horizontal z-chains are built, then the vertical xy-grids are built. The total number of beads can thus be split into two contributions: $N_{beads} = N_{beads,z} + N_{beads,xy}$. In order to avoid double counting, the crosslink beads are counted as being only part of the z-chains.
The number of beads per z-chain is given by N_z. The number of z-chains is given by the number of crosslinks in the xy-directions squared, such that the total number of beads in the z-chains is

given by $N_{beads,z} = N_{c,xy}^2 N_z$.
When building the *xy*-grids, one has to avoid double counting the crosslink beads. So, when counting the additional beads in those *x* and *y* chains, one has to drop the crosslink beads. The *x*- and *y*-chains at a given *z* coordinate are viewed as constituting one *xy*-grid. Then there are a total of $N_{c,z}$ *xy*-grids in the network. The number of beads per *x*-chain, while avoiding double counting the crosslink beads, is given by $N_{xy} - N_{c,xy}$. The same applies to the number of beads per *y*-chain. In each *xy*-grid, there are $N_{c,xy}$ *x*-chains and $N_{c,xy}$ *y*-chains. This gives $2N_{c,xy}(N_{xy} - N_{c,xy})$ beads per *xy*-grid, and a total of $N_{beads,xy} = 2N_{c,xy}(N_{xy} - N_{c,xy})N_{c,z}$ in the whole network.
The total number of beads in a network is therefore given by:

$$N_{beads} = 2N_{c,xy}(N_{xy} - N_{c,xy})N_{c,z} + N_{c,xy}^2 N_z \ .$$

For implementing the interactions within in the network and the interactions between cell and network later, one needs (i) a *chain list* containing all nearest neighbour bond IDs in this chain, and (ii) a *bond list* containing the bond partner IDs for a given bond ID. The number of polymer chains along the *z*-direction is given by $N_{c,xy}^2$, while the number of polymer chains in the *xy*-grids is given by $2N_{c,xy}N_{c,z}$. The number of nearest neighbour bonds in a chain with *m* members is given by *m-1*. Therefore, the number of bonds is given by the number of chains times the beads per chain minus 1, respectively. This gives:

$$N_{bonds} = N_{c,xy}^2(N_z - 1) + 2N_{c,xy}N_{c,z}(N_{xy} - 1) \ .$$

The network can be viewed as consisting of individual network chains, which are crosslinked. The network interactions act between neighbouring beads within a chain. Due to the crosslink beads which are part of three chains each, the chains are linked forming one network. The following derivations always consider interactions within an individual chain.

Finitely extensible nonlinear elastic (FENE) bond interactions

The attractive part of the bond interaction between two polymer beads in a chain is modeled using a FENE potential. The corresponding bond vector between beads *i* and *j* is again given by $\vec{r}_{ij}$. The interaction strength is given by k_F, while the bond length $r_{ij} \equiv |\vec{r}_{ij}|$ is effectively restricted by the maximum displacement Δr_{max}. Let B_c be the set of neighbour bonds of the respective chain and B_{c_i} be the set of bonds bead *i* contributes to. The total potential then reads:

$$U_F = \sum_{ij \in B_c} [\ -\frac{k_F}{2}\ \Delta r_{max}^2\ \ln[1 - (\frac{r_{ij}}{\Delta r_{max}})^2]\ ] \ . \tag{2.44}$$

It should be noted that the logarithm is only defined for positive arguments. For the following force computation, it is therefore assumed that $r_{ij} < \Delta r_{max}$. The force contribution within chain c on bead *i* is thus :

$$\vec{F}_{F,i} = -\vec{\nabla}_i U_F = -\vec{\nabla}_i \sum_{ij \in B_{c_i}} [\ -\frac{k_F}{2}\Delta r_{max}^2 \frac{1}{1 - (\frac{r_{ij}}{\Delta r_{max}})^2}\ ]\ [\ -2\frac{r_{ij}}{\Delta r_{max}}\ ]\ \frac{1}{\Delta r_{max}}\vec{\nabla}_i r_{ij} \tag{2.45}$$

This gives the force expression:

$$\vec{F}_{F,i} = k_F \sum_{ij \in B_{c_i}} [\ \frac{r_{ij}}{(\frac{r_{ij}}{\Delta r_{max}})^2 - 1}\ ]\ \hat{\vec{r}}_{ij} \tag{2.46}$$

For $r_{ij} < \Delta r_{max}$, the denominator in the force contribution is negative such that the force tries to decrease r_{ij} towards zero. As r_{ij} approaches Δr_{max}, the denominator approaches zero, such that the resulting force contribution tends to $\pm\infty$.
The equilibrium distance of such a FENE bond is zero. In the simulations, however, each FENE potential is accompanied by a repulsive WCA potential, such that the effective equilibrium distance has a non-zero value.

Weeks-Chandler-Andersen (WCA) interactions

The repulsive part of the bond interaction between two polymer beads is modeled using a Weeks-Chandler-Andersen (WCA) potential. Additionally, the repulsive interactions between membrane nodes and polymer beads are modeled using a WCA potential. The following derivations are considered for two general particles *i* and *j*. It then applies to the interactions between two polymer beads as well as the interactions between membrane node and polymer bead. Let B be the set of all bonds and B_i be the set of the bonds particle *i* contributes to .
A WCA potential is a truncated and shifted Lennard-Jones potential. The Lennard-Jones potential (LJ) is a popular potential used to model realistic molecular interactions:

$$U_{LJ} = 4\epsilon\ [\ (\frac{\sigma}{r_{ij}})^{12} - (\frac{\sigma}{r_{ij}})^{6}\ ]\ . \tag{2.47}$$

The parameter σ is a measure for the size of the interacting particles, defining the location of the minimum of the potential at $r = 2^{1/6}\sigma$. The parameter ϵ defines the potential depth and thus measures the strength of the interaction. The WCA represents the purely repulsive part of this interaction. It is an LJ potential which is cut off at the minimum and shifted to the top such that the energy and force are smooth at $r = 2^{1/6}\sigma$. The total WCA interaction potential can be written as $U_{WCA} = \sum_{ij \in B} U_{WCA,\,ij}$ with the individual contributions being defined as:

$$U_{WCA,\,ij} = \begin{cases} 4\epsilon\ [\ (\frac{\sigma}{r_{ij}})^{12} - (\frac{\sigma}{r_{ij}})^{6} + \frac{1}{4}\ ] & \text{for } r_{ij} \leq 2^{1/6}\sigma \\ 0 & \text{else} \end{cases} \tag{2.48}$$

In the following, the force on particle *i* from a single bond with particle *j* is considered. For $r_{ij} \geq 2^{1/6}\sigma$, the resulting force is zero. Assuming $r_{ij} < 2^{1/6}\sigma$, the resulting force can be computed as:

$$\vec{F}_{WCA,i} = -\vec{\nabla}_i U_{WCA} = -4\epsilon\ [\ \vec{\nabla}_i(\frac{\sigma}{r_{ij}})^{12} - \vec{\nabla}_i(\frac{\sigma}{r_{ij}})^{6}\ ] \tag{2.49}$$

To unclutter notation, for the following line r_{ij} is rewritten to be $r \equiv r_{ij}$. The index of *r* is then free to denote its Cartesian components. Then:

$$\vec{\nabla}_i(\frac{1}{r^m}) = \vec{\nabla}_i(r_l r_l)^{-\frac{m}{2}} = -\frac{m}{2}(r_l r_l)^{-\frac{m}{2}-1}\vec{\nabla}_i(r_l r_l) - \frac{m}{2}(r_l r_l)^{-\frac{m+2}{2}} 2r_i = -\frac{m}{r^{m+2}}\vec{r}\ . \tag{2.50}$$

Changing back notation, this yields:

$$\vec{F}_{WCA,i} = \epsilon \, [\, 48(\frac{\sigma^{12}}{r_{ij}^{14}}) - 24(\frac{\sigma^{6}}{r_{ij}^{8}}) \,] \, \vec{r}_{ij} \;=\; \epsilon \, [\, 48(\frac{\sigma}{r_{ij}})^{12} - 24(\frac{\sigma}{r_{ij}})^{6} \,] \, \frac{\vec{r}_{ij}}{r_{ij}^{2}} \tag{2.51}$$

Therefore, the final force contribution of the bond between *i* and *j* on *i* for $r_{ij} < 2^{1/6}\sigma$ can be written:

$$\vec{F}_{WCA,i} = \epsilon \sum_{ij \in B_i} [\, 48 \, (\frac{\sigma}{r_{ij}})^{12} - 24 \, (\frac{\sigma}{r_{ij}})^{6} \,] \, \frac{\vec{r}_{ij}}{r_{ij}^{2}} \, . \tag{2.52}$$

The term in brackets in the force contribution is always positive. Combined with the distance vector after the bracket, one can verify that the force contribution pushes both interacting particles *i* and *j* away from each other, as one would expect from a purely repulsive potential. WCA interactions were implemented to act between all nearest neighbour pairs in each polymer chain, as well as between all pairs of membrane node and polymer bead.

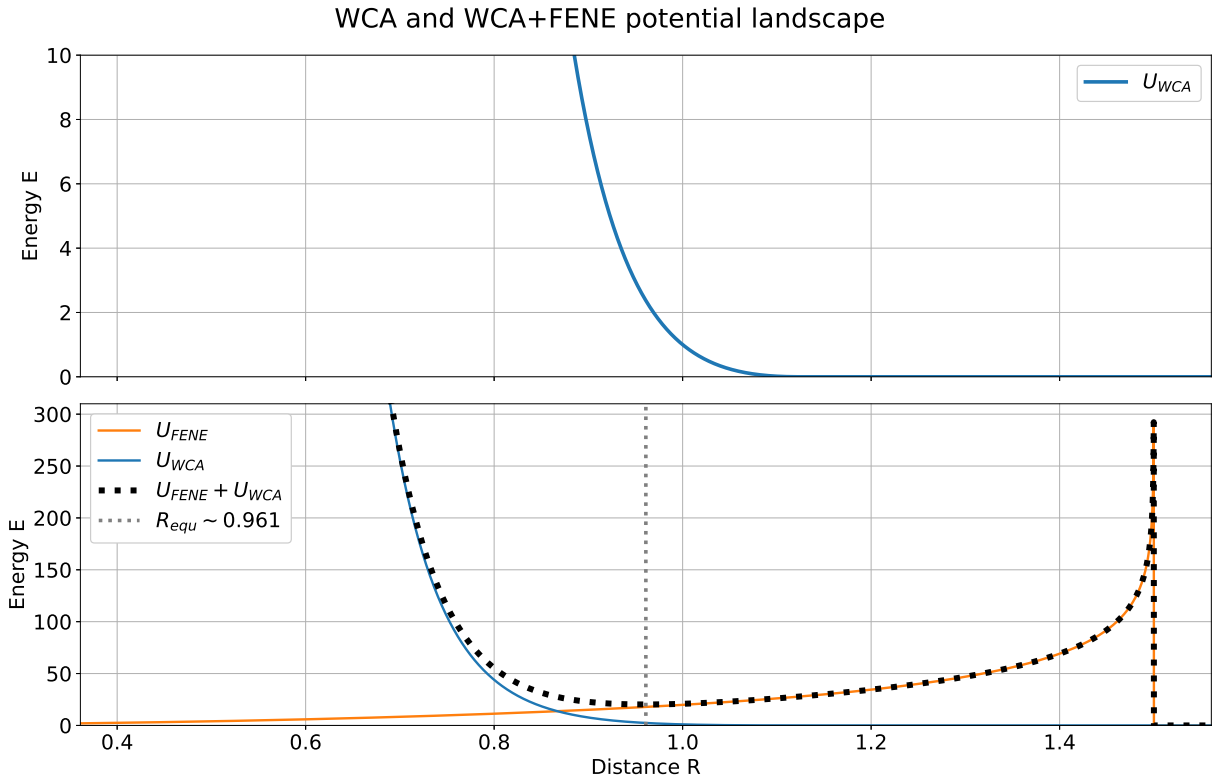

Figure 2.6: Visualization of the energy landscapes of WCA and WCA+FENE potentials for $\sigma_{WCA} = \epsilon_{WCA} = 1$, $k_{FENE} = 30$ and $\Delta r_{max,FENE} = 1.5$. Those particular parameters are inspired by the Kremer-Grest model [25].

Figure 2.6 shows the energy landscape of both WCA and FENE+WCA potentials. The visualized potentials use the parameter values $\sigma_{WCA} = \epsilon_{WCA} = 1$, $k_{FENE} = 30$ and $\Delta r_{max,FENE} = 1.5$. These are the numerical values which were also used in the simulations of this project. The first plot, showing the pure WCA interaction potential, models the interactions between membrane nodes and polymer beads. One can see that there's already a weak potential gradient for $R > 1$.

However, in simulations membrane nodes and polymer beads could "overlap" for a short period of time before the potential gradient is strong enough to push them apart. The second plot, showing the combination of both WCA and FENE potential landscapes, models the interactions between two polymer beads. One can see that, using the discussed parameter values, the equilibrium distance R_0, representing the minimum of the combined WCA and FENE potential, is located at a numerical value of about 0.961, slightly below *1*. It should also be noted that for $R > \Delta r_{max,FENE} = 1.5$ the WCA potential is zero while the FENE potential is not defined.

Bending interactions for a polymer chain

The bending elasticity of an individual polymer chain in a polymer network can be simulated by constraining the bond lengths between neighbouring beads, while including a potential for variations in the bond angles.
Such a potential for variations in the bond angle θ should be symmetric and periodic in θ. This is satisfied for a potential which only depends on the angle's cosine, such that $U(\theta) = U(\cos\theta)$. One potential is included for each bond angle of the chain. So for a chain with *m* members, one obtains *m-1* angles between nearest neighbours. Using an energy penalty quadratic in displacements of $\cos\theta$ leads to:

$$U_{Bend,\,NW} = \sum_{i=1}^{m-1} \frac{k_{Bend,\,NW}}{2} (\,\cos\theta_i - \cos\theta_0\,)^2\ . \tag{2.53}$$

The parameter $\cos\theta_0$ defines the spontaneous curvature and was chosen to be $\cos\theta_0 = 1$ such that the minimum energy configuration is a straight chain. One can define the distance vectors between neighbouring beads: $\vec{d}_i \equiv \vec{r}_i - \vec{r}_{i-1}$. The cosine can then be calculated as:

$$\cos\theta_i = \frac{\vec{d}_i \cdot \vec{d}_{i-1}}{|\vec{d}_{i|} \cdot |\vec{d}_{i-1}|} \tag{2.54}$$

The position vector of bead *i* will therefore appear in the potentials of the angles θ_i, θ_{i+1}, and θ_{i+2}. The force on bead *i* can thus be calculated as:

$$\vec{F}_i = -\vec{\nabla} \sum_{k=i}^{i+2} \frac{k_{Bend,\,NW}}{2} (\,\cos\theta_k - \cos\theta_0\,)^2\ . \tag{2.55}$$

The exact expression of the resulting force contributions can be found in [26]. Each polymer bead then has force contributions from its two nearest neighbours. The boundary beads, having only one neighbour, only have one force contribution, while the crosslink beads, participating in three bonds, have six force contributions. The essential point is that one ends up with an analytical expression to compute the resulting bending forces on bead *i* from knowledge of the positions of all polymer beads:

$$\vec{F}_{Bend,i} = [-\vec{\nabla}_i U_{Bend}]\ (\vec{r}_1, ...\vec{r}_i, ...\vec{r}_N)\ \ . \tag{2.56}$$

2.4 Units and code structure

In the simulations, the numerical values of the thermal energy k_BT, the mean initial bond length of the cell surface edges b_0 (see figure 2.3b), and the diffusion constant D_0 of a single node were chosen to have a numerical value of 1. This means all energies are measured in units of the thermal energy, lengths are measured in units of the mean initial bond length, and time is measured in units of $\frac{b_0^2}{D_0}$. The latter represents the diffusive timescale of an individual node. The time step was chosen to be $\Delta t = 10^{-4}$ in all simulations. In the visualized plots in the results, time is plotted in simulation units if the plots are regarded as simulation results. For estimation of equilibration times or investigations relevant for parameter choices, time is plotted in time steps, since this is the relevant quantity for the simulation setup. Choosing the units as described above, with a Delaunay triangulation of factor 10, results in a cell surface model with a radius of about $R_{cell} \sim 7.9$.

In the course of this project, a code for the simulation of driven deformable cells in deformable polymer networks was written. The code can be roughly structured into two parts. The first part concerns the generation of the initial system. This includes defining all the relevant parameters, generating the initial position coordinates of both cell nodes and network beads as well as generating all the arrays containing the information necessary for the following force computations. The second part concerns the time evolution of the system. For each time step, force computations and the subsequent numerical integrations of the equations of motion are performed. The total force vectors on each particle are computed accounting for the cell interactions, cell-network interactions, network interactions as well as the external driving force. The position updates are done using the GB algorithm [17]. During each time step or in periodic intervals, relevant parameters like positions, forces or energies can be stored in external files for data analysis purposes.

The code sections for the Delaunay triangulation as well as for the bending force computations of both cell surface nodes and polymer beads were already implemented and provided by the co-supervisor of this thesis, Dr. Andreas Zöttl. The rest of the simulation code was written from scratch in the course of this project.

Chapter 3

Results and Discussion

The results are discussed in 3 subsections. The first subsection discusses different cell models by investigating the impact of different cell surface interaction potentials on relevant properties of the cell surface. The second subsection presents the results from simulations of driven deformable cells in rigid networks. This includes a discussion of the generic cell behaviour and an investigation of the influence of relevant parameters on the cell behaviour. The third subsection presents results from a simulation of driven deformable cells in deformable networks.

3.1 Cell models

Equilibration

The Brownian dynamics integrator is used to simulate cell motion in a thermal environment of a given temperature T. However, the surface nodes are initialized with zero velocity. The cell surface is therefore effectively a system initially at zero temperature which is brought into contact with a heat bath of non-zero temperature. The cell then equilibrates approaching thermal equilibrium and the temperature of the heat bath. The cell can be viewed as equilibrated when all energy contributions fluctuate around a constant plateau value. Figure 3.1 shows a visualization of the shape evolution of the triangulated surface of a minimal cell model including only bond and bending potentials ($k_{Bond} = 10^2$, $k_{Bend} = 1$). The cell on the left shows the initial configuration, the one in the middle shows the configuration after just a few time steps, while the right one shows the equilibrated cell surface after a few thousand time steps. It should be noted that the shown bonds in the visualization were automatically drawn between particles in VMD and do not necessarily represent the actual triangulation. Nonetheless, the visualization is useful to show the evolution of the general surface structure. The chosen interaction potentials are relatively weak, that is why the equilibrium surface fluctuations are relatively strong.

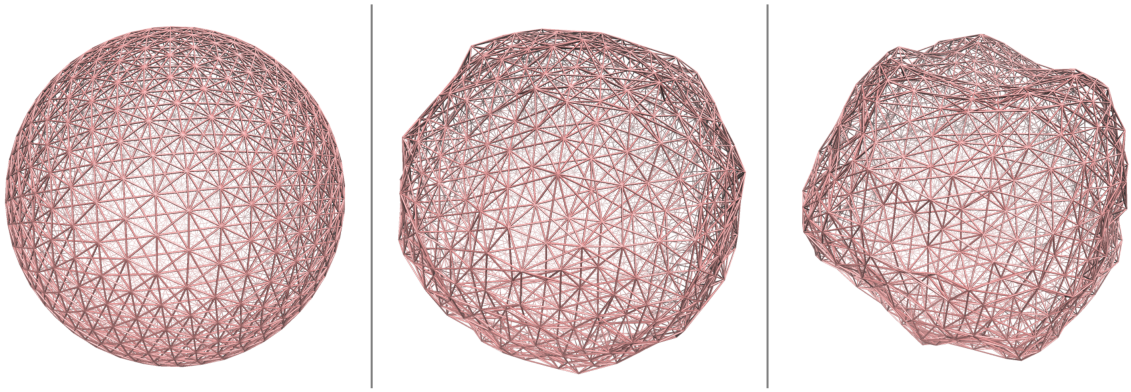

Figure 3.1: Time evolution of the cell surface structure, using a minimal cell model including only bond and bending potentials ($k_{Bond} = 10^2$, $k_{Bend} = 1$).

Impact of different potentials

Figure 3.1 shows that the equilibrium cell surface deviates from the initial surface. In general, this also depends on the chosen interaction parameters. In order to show the impact of adding different potential contributions, the bond length distributions as well as the volume, and area time evolution were investigated for 4 different cell models, as shown in figure 3.2. The first model only includes bond potentials, while the other three each add one yet different contribution: bending, volume, or area potentials, respectively. The interaction strengths are shown in the figure. The simulations were run for 100.000 time steps, while measurements such as volume, surface area, and bond lengths were taken every 200 time steps. The shown distributions were averaged over the last 200 measurements. The distributions are plotted as probability densities, while both area and volume values are normalized to their respective initial value.
The top plot in figure 3.2 shows the distribution of the deviations of the surface bond lengths from their respective initial value. For this curve, the deviations of individual bond lengths from their respective initial value were taken, averaged over time, and then transformed into a smooth curve using a Gaussian kernel density estimator. Considerations from statistical mechanics show that the distribution of an isolated single bond in a thermal environment and subjected to an interaction potential follows a Boltzmann distribution, with the distribution width being determined by the potential strength k_{Bond}. This means for the distribution of the bond length deviations Δb:

$$P(\Delta b) \;\propto\; \exp\left\{-\frac{U_{Bond}}{k_B T}\right\} \;\propto\; \exp\left\{-k_{Bond}\,(\Delta b)^2\right\}. \tag{3.1}$$

This gives a first approximation for how the bond length distribution should look like. Since the surface bonds are not isolated, their distribution should deviate from equation 3.1, but show a similar trend. The top plot in figure 3.2 shows that the simulation including only bond interactions produces a bond length distribution quite similar to the Boltzmann approximation. The deviation can be explained by the fact that the surface bonds are not isolated such that the individual bond potentials are not independent. Comparing the curve of the first simulation including only bond interactions to the other three shows the impact of the different potentials, explained in the following. The chosen plots are meant to show the qualitative impact of the different potentials using a particular set of interaction strengths, while the precise quantitative impact also depends on the chosen interaction strengths.
Including a bending potential slightly narrowed the distribution, which can be explained by the

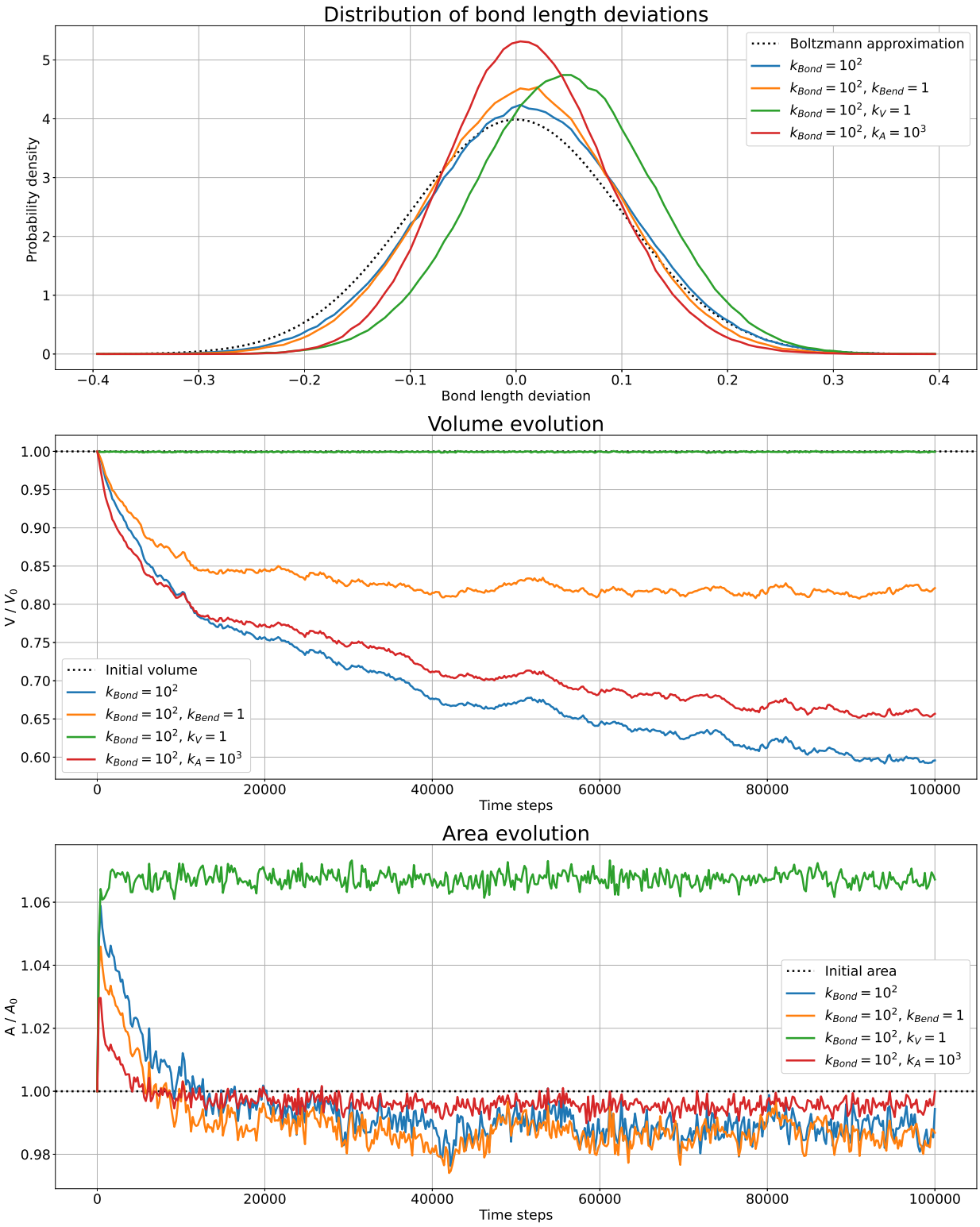

Figure 3.2: The influence of adding different potential contributions on the equilibrium bond length distributions, as well as the volume and area time evolution. Each plot shows the simulation results of four minimal cell models, taking into account bond interactions with one additional yet different type of interaction potential each. The legend shows only the non-zero force constants of the respective model.

minimal energy configuration of the bending potential being a flat surface. This limits the bond length fluctuations. Including a volume potential accounting for constant volume resulted in a narrower but also shifted distribution. The narrowing can be explained by the fact that the volume potential introduces an additional energy penalty for bond lengths deviating from their initial value. The shifting of the distribution to the right can be explained by a non-linear interplay between volume and bond potentials. A bond length deviation including a position displacement orthogonal to the triangulated surface results in a volume displacement, which leads to an energy penalty. However, a bond length displacement directed towards the cell outside leads to a smaller volume displacement and thus a smaller energy penalty than the same bond length displacement directed towards the cell inside. This is a result of the reference configuration being a curved surface. This effect could be seen as an explanation of the asymmetric impact of the volume potential on the bond length distribution. This, however, does not necessarily explain why the peak value of the distribution changes. Including area interaction potentials also resulted in a narrower distribution. Similarly, this can be explained by the additional energy penalty for a bond length displacement. In contrast to the volume potential, the impact of the area potential is symmetric since the direction of the displacement does not influence its energy penalty.
It should be noted that in these simulations the initial area and surface were taken as reference values for the area and volume interaction potential, respectively. One could in principle simulate osmotic pressure by changing the values of the reference volume. Choosing a larger reference value could be used to simulate an effective hypotonic environment, while a smaller value could be used to simulate an effective hypertonic environment.

It is apparent in the middle plot of figure 3.2 that the cell model including only bond interactions does not conserve the initial volume. In fact, this model eventually shrinks down to a clump of below 5 percent of the initial volume (this takes more than the 100.000 time steps shown in the figure). Including area interactions, the volume conservation appears to be slightly better. This can be explained by the fact that for a sphere, area increase/decrease also implies volume increase/decrease. Including bending interactions, one can see that the volume drops from the initial value but approaches a plateau value once the cell is equilibrated. Considering the flat sheet as the minimum energy configuration of the bending potential, this behaviour can be motivated by the bending potential providing the necessary outward pressure to prevent the shrinking of the surface. Including a volume potential, one can see that the initial volume is conserved extremely well.

The bottom plot of figure 3.2 shows the area evolution of the different models. Interestingly, including volume interactions resulted in an apparent equilibrium plateau surface area which is larger than the initial surface area. This is caused by the thermal equilibrium bond length fluctuations combined with the constraint of constant volume. For the other three models, the area peaks at the beginning, then decreases and roughly approaches a plateau value below the initial value. In those cases, the thermal equilibrium bond length fluctuations have a similar effect, however, the area is conserved better at the cost of the volume conservation. The most efficient surface area conservation is achieved for the model including the additional area potentials.

Driven cells in a fluid

The different interaction potentials should not have a significant impact on the velocity evolution of a driven cell's center of mass in a fluid. The velocity evolution was therefore investigated for different constant external force strengths using a cell model including only bond interactions. Inserting the diffusion constant of an individual node $D = 1$ and the thermal energy $k_B T = 1$ into equation 2.2 shows that in this case the numerical values of the driving force and the resulting terminal velocity are equivalent. Figure 3.3 shows the evolution of the projection of the cell's center of mass velocity in the direction of the driving force, normalized to the respective terminal velocity v_t. The direction of the driving force is denoted by the z-direction. The projection of the velocity in this direction is called the speed v_z. One can see that in all four cases the measured speed fluctuates around the value of the respective terminal velocity. The fluctuations of all cases are synchronized, since all simulations used the same seed number for the random number generation. For small external forces, the thermal fluctuations still play a dominant role resulting in large relative speed fluctuations. The impact of the thermal fluctuations decreases, however, for increasing external force strengths.

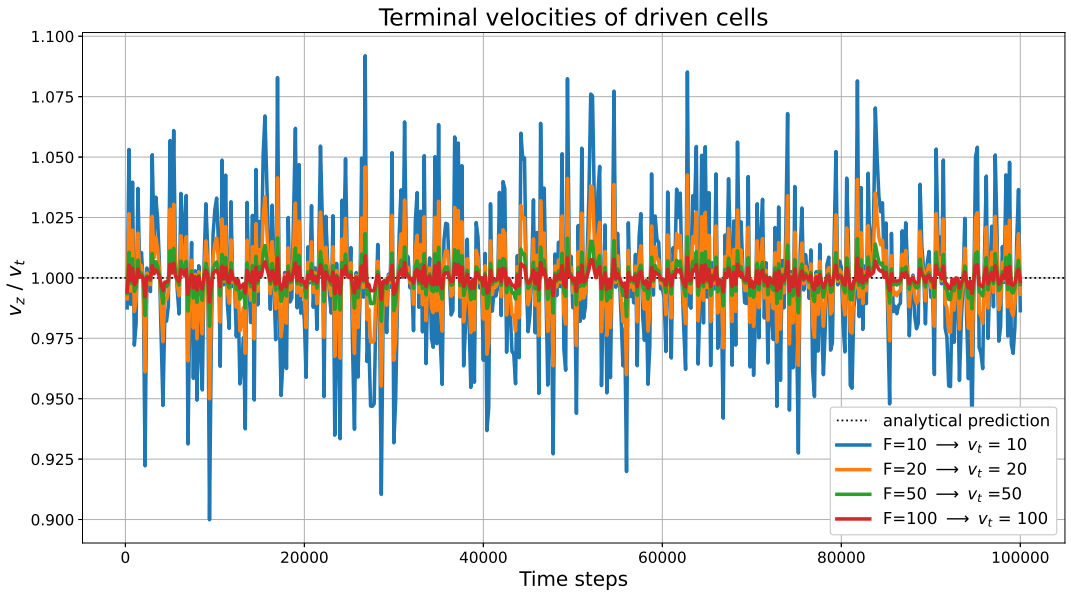

Figure 3.3: Speed evolution of driven cells in a fluid, normalized by the corresponding analytically predicted terminal velocity.

3.2 Driven deformable cells in rigid networks

In order to get a first overview of the generic behaviour of a driven deformable cell squeezing through a network, simulations were run with a rigid network. This means the network beads take part in interactions with cell nodes but their positions stay fixed. The distance between two neighbouring beads was chosen to be equal to the mean initial bond length between two neighbouring cell surface nodes $b_{beads} = b_{nodes,0} \equiv b_0 = 1$. Using a rigid network, simulations of driven cells were found to be stable for network grid sizes larger or equal to 12 in a certain range of cell surface interaction parameters. Simulating the network as a rigid body also allows to reduce the size of the network which reduces the computational cost of each simulation. Since all network beads stay at a fixed position, there are no boundary effects to worry about. Therefore, the network can be initialized as only one channel through which the cell can be pulled ($N_{cells,xy} = 1$). The length of the network was set to $N_{cells,z} = 10$. It should be noted that, while the network has 10 network cells along the z-direction, it effectively has 11 pores.

Generic behaviour

Using only bond and bending potentials, the cell surface deforms at the first pore, shrinking to a size small enough to move through the rest of the network without any significant interactions with the network. This can be seen in the example system using $k_{Bond} = 500$, $k_{Bend} = 1$, and $a_{grid} = 13$, which is visualized in figure 3.4. Instead of all network beads, only the bonds between neighbouring network beads are shown such that the cell is clearly visible going through the network. However, additional bonds around the crosslink beads were automatically drawn in VMD which do not represent physical bonds. This also applies to the following network visualizations. The shrinking process at the first pore can be seen going from snapshot 2 to 3. Snapshot 4 shows that at the next pore the cell is small enough to avoid significant interactions with the network.

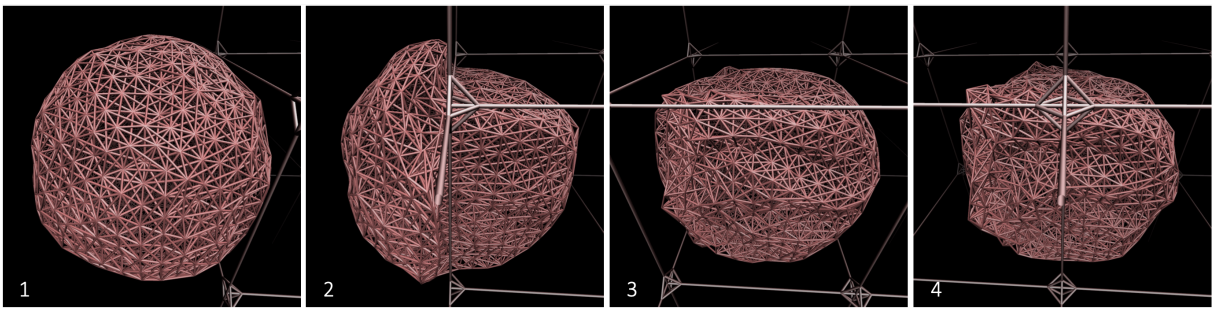

Figure 3.4: Visualization of cell model using only bond and bending potentials.

Therefore, in order to represent more realistic cell behaviour, a volume potential was included. This reproduced a squeezing behaviour where the cell needs to squeeze through each pore by deforming its surface. However, simulations using those three types of cell interaction potentials were found to be stable only for particular combinations of interaction strengths. Additionally including area potentials allowed to simulate the system without surface bond instabilities for a broader range of parameter combinations. As shown in table 3.1, a particular set of parameters is used to discuss different cell properties in the following: $k_{Bond} = 10^3, k_V = 1, k_A = 200, k_{Bend} = 100, a_{grid} = 12$. This example can be used to discuss the generic behaviour of an externally

driven deformable cell in a rigid network with a cell size larger than the pore size.

k_{Bond} / (k_BT/b_0^2)	10^3
k_{Bend} / (k_BT/b_0)	100
k_V / (k_BT/b_0^6)	10
k_A / (k_BT/b_0^4)	200
σ_{WCA} / b_0	1
ϵ_{WCA} / k_BT	1

Table 3.1: Interaction parameters used to investigate the generic cell behaviour when having to squeeze through network pores. The first four parameters are cell surface interaction parameters while the last two define the interactions between cell surface nodes and network beads.

The system's behaviour is affected by thermal noise. Therefore, in order to obtain significant results, it is necessary to perform an ensemble of simulations using different seed numbers for the random number generation. Then one can use ensemble-averages to determine relevant quantities. An ensemble of 10 systems was run for 10^5 integration steps with 10^3 measurement steps, such that relevant quantities were measured every 100 integration steps. The cells were initialized at a z-distance of $a_{grid} + 10$ from the first network pore, and at x- and y- coordinates such that the cell's center of mass is pulled exactly through the center of the pores. The following discussion of the cell surface behaviour always refers to ensemble-averaged properties. The ensemble-averaged time series like the evolution of energies are simply sample means at each time step. Single ensemble-averaged mean values, like the mean speed when translocating through a pore, were obtained as sample means of the respective mean values of the individual simulations. The error $\hat{\sigma}$ of such point estimates $\hat{\mu} = \overline{x} \equiv \sum_{i=1}^{N} x_i$ for some true value μ can thus be approximated by $\hat{\sigma}^2 = \frac{\sigma^2}{N}$ with σ being the standard deviation of the sample of means x_i and N being the sample size.

Figure 3.5 shows the projection of the velocity of the cell's center of mass in the direction of the driving force, now referred to as the speed v_z. The top plot shows the cell speed in its full extent while the bottom plot shows the top region of the oscillations in more detail. The local speeds were determined by calculating the distance between the position at the last time step and the position at the current time step. The ensemble-averaged curve was then obtained by averaging over the values of each individual simulation at each time step.
The top plot clearly shows that the network pores act as barriers slowing down the cell. When encountering a network pore, the driven cell has to deform its surface and squeeze, such that the speed decreases to a minimum value and then increases again. The subsequent speed maxima after each pore exceed the terminal velocity of the respective cell in a network-free fluid. This indicates that in the squeezing process, elastic interaction energy is utilized to locally enhance the cell speed. The speed displays an overall oscillatory behaviour. However the curve looks less like a sinusoidal curve, but more like almost linear curves with discrete turning points at the minima and maxima.
For this particular set of interaction parameters, the cell speed in the network ranges from slightly below 0.6 to slightly below 1.1 in units of the corresponding terminal velocity, with a mean value of about 0.83 within the network. Interestingly, the peak values grow to values larger than 1.

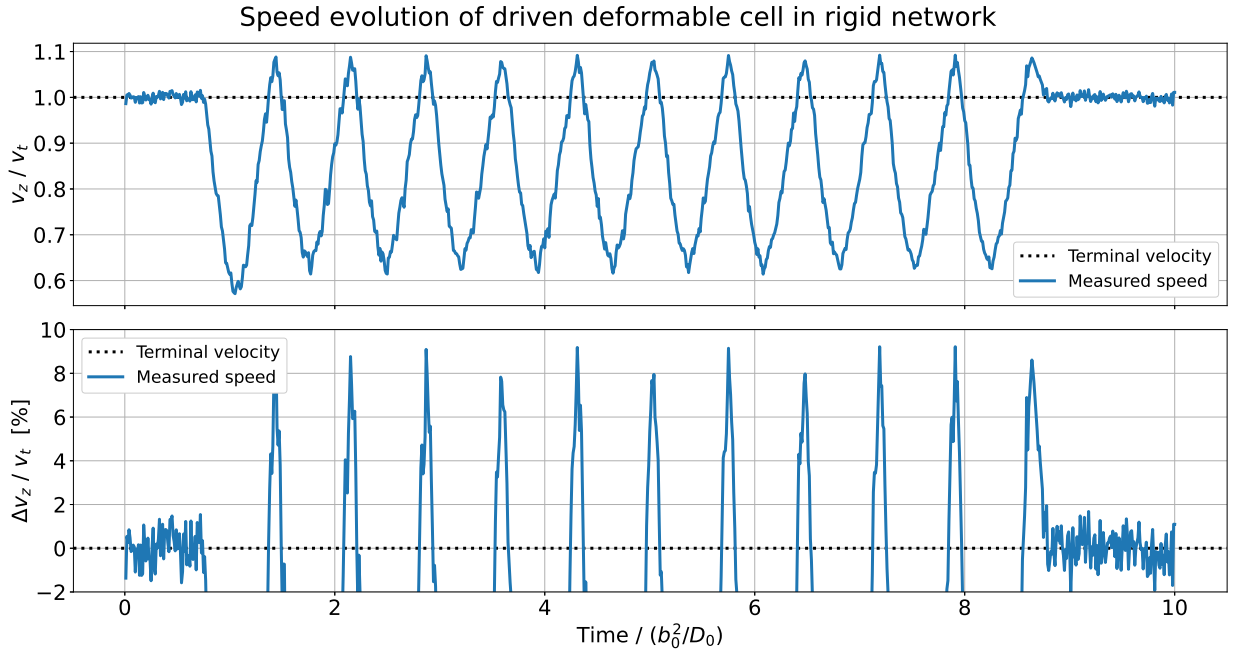

Figure 3.5: Speed evolution of a driven deformable cell in a rigid network. The top plot shows the speed normalized to the respective terminal velocity in a network-free fluid, while the bottom plot shows the speed enhancement with respect to the terminal velocity in a percentage measure.

The difference of the speed maxima after each pore and the terminal velocity can be taken as a measure for this observed speed enhancement. Figure 3.5 shows the speed enhancement $\Delta v_z \equiv \langle v_{z,peak} \rangle - v_t$ after a pore, normalized to the terminal velocity and plotted as a percentage measure. In this case, the speed enhancements after the pores fluctuates between about 8 and 9 %. After the last pore of the network, the cell speed returns to fluctuating around the terminal velocity.

Figure 3.6 represents the time evolution of the different energy contributions. The top plot shows the energy evolution using a logarithmic y-axis due to the different orders of magnitude. One can see pronounced oscillatory behaviour of all energy contributions with maxima and minima appearing at similar points in time. A closer look reveals that some contributions look synchronized while others appear to have a constant phase shift. The WCA and bending energies appear to be synchronized, while the volume and area interaction energies as well as the bond energies seem to be also synchronized. However, a slight phase shift between these two groups is visible. In order to quantify this phase shift, the bond and WCA energies were fitted using a sinusoidal fit function $f(t) = a \sin(\omega t + \phi) + f_0$. The obtained phase difference $\Delta\phi$ in degrees can then be converted to a time quantity via $T_{shift} = \frac{\Delta\phi}{360} \frac{T_{out} - T_{in}}{10}$. The parameters T_{in} and T_{out} represent the points in time when the cell's center of mass enters and leaves the network, respectively. Therefore, $\frac{T_{out} - T_{in}}{10}$ represents the average time it takes the cell to travel through one of the ten network cells. The transformation assumes that one oscillatory period of 360 degrees corresponds to the cell travelling through one network cell. The time shift was then calculated to be about 505 ± 5 time steps. It should be noted though that the energies were measured only every 100 time steps which, due to the size of the time shift, constrains its precision. The bottom plot in 3.6 shows the measured as well as fitted curves of both WCA and bond energies such that

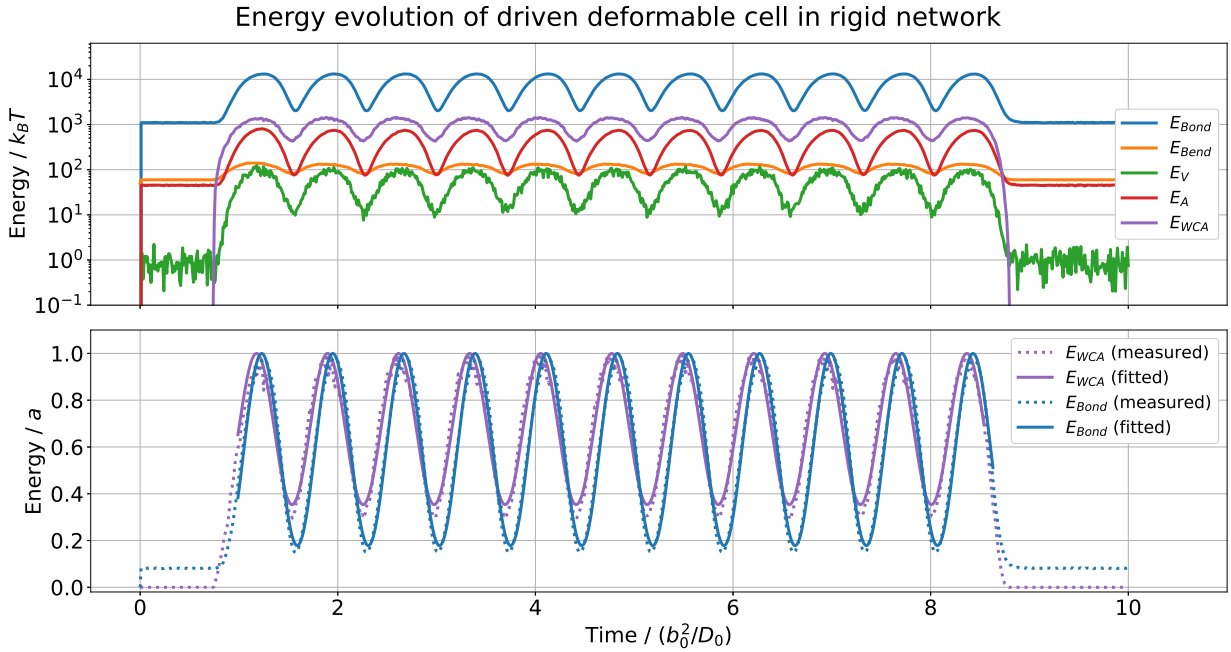

Figure 3.6: Energy evolution of a driven deformable cell in a rigid network. The top plot shows the time evolution of the relevant energy contributions using a logarithmic y-axis, while the bottom plot shows the measured WCA and bond energies with sinusoidal fits, normalized to the fitted amplitude a.

the slight phase shift is visible. For visualization purposes, the curves were normalized by the respective fitted oscillation amplitude, such that both curves peak at the value of 1.

Figure 3.7 represents the time evolution of the cell surface shape. The top and middle plots show the cell volume and surface area evolution, normalized to the respective initial value. One can see that, within the network, the cell surface increases periodically. The surface area has to increase when encountering a pore due to the necessary cell surface squeezing. The surface area minima are still larger than the equilibrium value since the cell surface cannot return to its equilibrium shape between two pores, since the pore size is smaller than the cell size. The cell volume on the other hand periodically decreases due to the cell squeezing. Due to the choice of interaction parameters, the relative deviations of the cell volume are below 1 percent, while the surface area deviations reach up to 10 percent. The time evolution of both volume and surface area should in principle depend on the choice of k_V and k_V.
The bottom plot shows the so-called normalized asphericity parameter. This is a parameter quantifying the deviations of the surface shape from the initial perfect sphere. First, the gyration tensor of the cell surface is determined:

$$g_{ij} = \frac{1}{N}\sum_{k=1}^{N} \Delta r_i^k \Delta r_j^k \ . \tag{3.2}$$

Here, *k* denotes the respective node and *i* and *j* denote the Cartesian components. The relative vectors are defined as $\Delta\vec{r} \equiv \vec{r}^{\,k} - \vec{r}^{\,c}$ with $\vec{r}^{\,c} \equiv \frac{1}{N}\sum_{k=1}^{N} \vec{r}^{\,k}$ being the body's center of mass. The eigenvectors of the gyration tensor can then be calculated and used to determine the asphericity parameter b:

$$b = \lambda_z - \frac{1}{2}(\lambda_y + \lambda_x) \ . \tag{3.3}$$

In this case, the eigenvalues are sorted such that λ_z represents the largest eigenvalue. In order to get a measure which is independent of cell size, the asphericity can further be normalized to the radius of the cell. Since the dimension of the eigenvalues is length squared, the asphericity is divided by R_{cell}^2. A value of zero then corresponds to a perfect sphere, while a large value corresponds to a large deviation from the spherical shape. This calculation was performed for each time step. The time evolution of b/R_{cell}^2 in figure 3.7 shows that at the beginning of the simulation, the value already fluctuates around zero due to thermal fluctuations. Within the network, b/R_{cell}^2 oscillates between values of about 0.17 to below about 0.03. This mirrors the need for the cell surface to acquire a rather elliptical shape in order to translocate through network pores. Interestingly, slightly before the oscillatory behaviour, one can see a small bump in the bottom plot, where the asphericity increases but afterwards drops down to almost zero again. This is not an essential feature of the generic behaviour of a cell squeezing through a pore, but would still be an interesting point of further investigation.

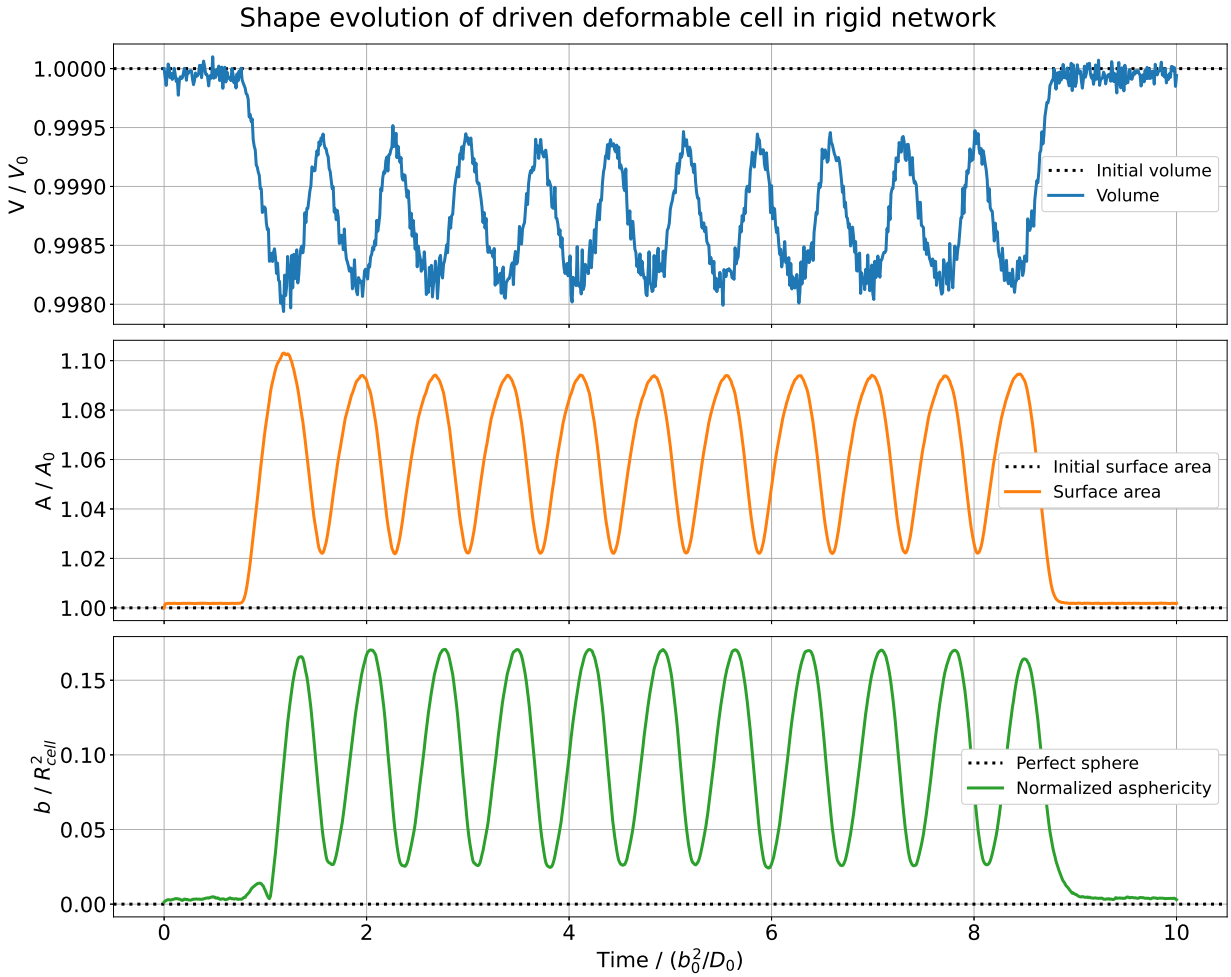

Figure 3.7: Shape evolution of a driven deformable cell in a network. The top and middle plot show the time evolution of the cell volume and surface area, both normalized to the respective initial value. The bottom plot shows the time evolution of the so-called normalized asphericity, measuring the deviation from the initial spherical surface shape.

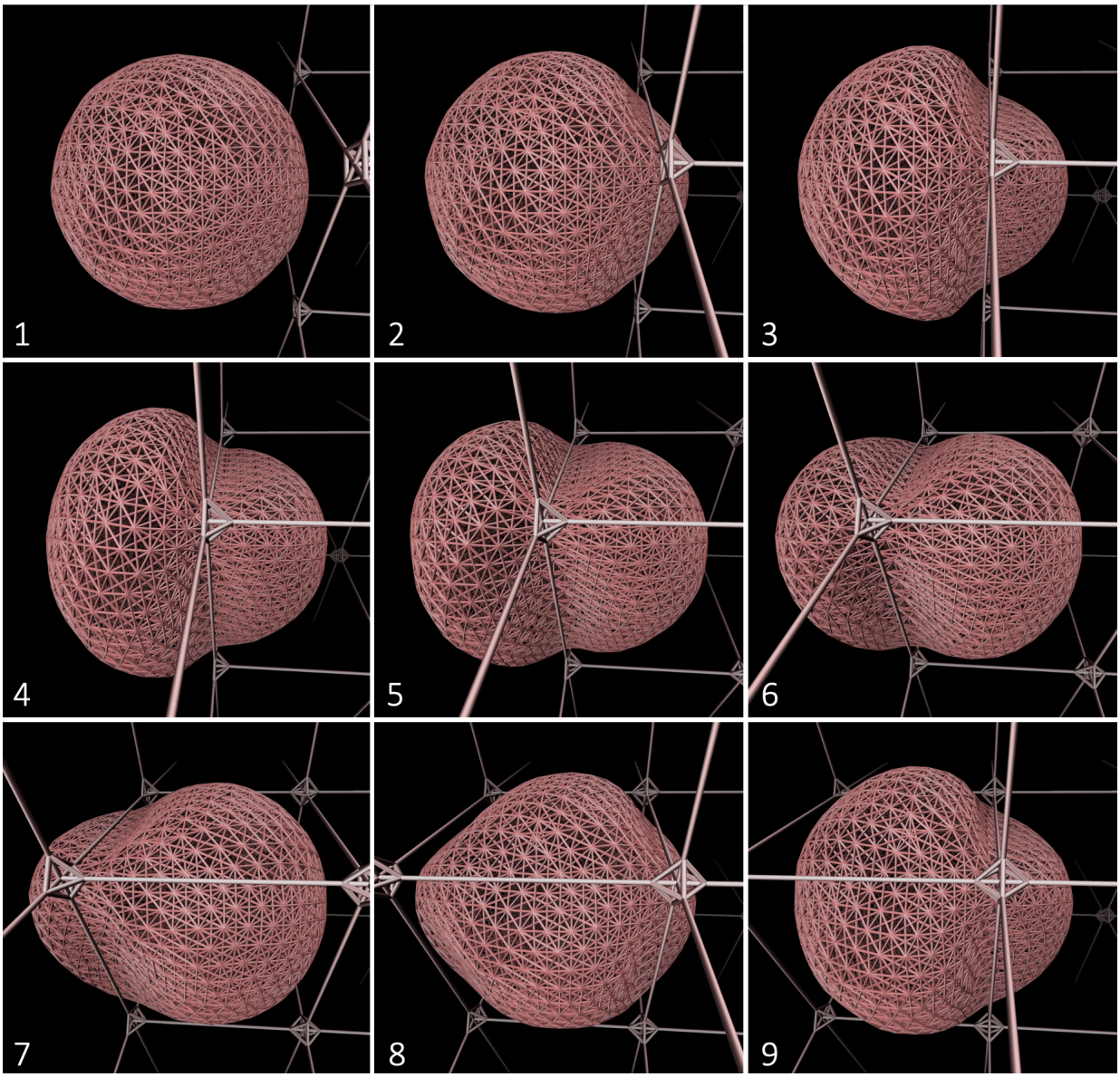

Figure 3.8: Visualization of the generic behaviour of a deformable cell in a rigid network.

Figure 3.8 shows a visualization of the the time evolution of the discussed example system. The 9 snapshots represent a time interval of 9600 time steps, such that 1200 time steps separate the different configurations. For a clearer visualization only the bonds are drawn of both cell surface and network chains. Although the drawn bonds do not exactly represent the triangulation and the network crosslink beads show additional bonds which are not part of the simulation, the visualization is still helpful to see the generic behaviour of the cell surface when squeezing through the first network pore.
Snapshot 1 represents the point in time when the cell speed starts to decrease due to interactions with the network beads. In the snapshot, the cell still seems to be rather far away from the network, but this is a visualization bias. The size of the network chains do not necessarily represent the actual size of the network beads in the simulation. The same applies to the cell surface nodes. Snapshots 2 and 3 show how the pore acts as a barrier, with the cell front translocating through the pore, while the rest of the cell body stays behind due to interactions

with the network. Snapshot 4 represents the cell speed minimum. The rear part of the cell body starts to squeeze through the pore leading to an increase in cell speed. Snapshot 5 represents the approximate configuration of the maxima of the energy contributions. Snapshots 5 and 6 also approximately represent the configuration when about half of the cell body has squeezed through the first pore. Snapshot 7 shows the configuration of the cell speed maximum. At this point, the rear part has successfully deformed such that it can translocate entirely through the pore. The stored elastic energy in the surface deformations has been converted to kinetic energy, leading to the local speed enhancement. Snapshots 8 and 9 show the cell encountering the next pore, which leads to a cell speed decrease and subsequent cell surface deformations.

In summary, figures 3.5, 3.6, 3.7, and 3.8 show the generic behaviour of a driven deformable cell squeezing through a rigid ordered network, using a particular set of interaction parameters. The results show oscillatory behaviour of many cell surface properties. Pores act like barriers transitionally slowing down driven cells. In the squeezing process, elastic interaction energy is utilized to locally enhance the cell speed after each pore. Additionally, a slight phase shift is visible between the different types of energy contributions. Considering its small value, however, this does not seem to be significant. The strength of these phenomena should in general also depend on the different system parameters. In order to investigate the influence of bending elasticity k_{Bend} and grid size a_{grid}, further simulations were run.

Influence of cell bending elasticity and pore size on cell behaviour

The introduced parameters of the mean cell speed and the speed enhancement after the pores were then investigated under the influence of a varying bending elasticity k_{Bend} and varying pore size. The pore size is given by the grid size of the ordered polymer network a_{grid}. However, this distance represents the length of a network unit cell, when viewing the network beads as point particles. Since membrane nodes and network beads see each other not as point particles, but as particles of diameter σ_{WCA} due to the implemented WCA interactions, this has to be taken into account. A better measure for the available free space for a membrane node within a network pore would therefore be the pore size $a_{grid}-\sigma_{WCA}$, and for the cell size $2R_{cell}+\sigma_{WCA}$. Therefore, the effective pore size relative to the cell size can be described by introducing the dimensionless pore size parameter: $\alpha \equiv \frac{a_{grid}-\sigma_{WCA}}{2R_{cell}+\sigma_{WCA}}$.
The influence of both parameters was investigated by keeping one of them fixed, while varying the second one. The values of the other cell interaction potentials remained unchanged with respect to the ones given in table 3.1. In order to investigate the influence of the bending elasticity k_{Bend}, the pore size was fixed at $a_{grid} = 12$, while k_{Bend} was varied between 0 and 200 using the values shown in table 3.2. In order to investigate the influence of the pore size, the bending elasticity was fixed at $k_{Bend} = 200$, while a_{grid} was varied between 12 and 19, as shown in table 3.3. For the simulations using $a_{grid} > 16$, the number of time steps was increased to 120.000 steps such that the cell still makes it through the whole network, while the ratio of time steps and measurement steps was kept constant.

In order to investigate the influences on the mean behaviour of the cell when encountering a pore, several properties were determined as an average over both the pores and the ensemble. Those properties were denoted with an asterisk, and are defined in table 3.4. Averaging over the pores

means that the respective time series was separated into 11 intervals with the length of one cell squeezing period each, such that each interval contains one of the 11 peaks and thus represents the time the cell spends at one pore. Those separated curves were then averaged to obtain one curve representing the mean squeezing behaviour for an individual simulation.

Fixed grid size a_{grid}/b_0	12
Corresponding α	0.63
Varied bending elasticity $k_{Bend}/(k_BT/b_0)$	0, 1, 25, 50, 75, 85, 90, 100, 125, 150, 200

Table 3.2: Parameters used to investigate the influence of the bending rigidity on the cell behaviour.

Fixed bending elasticity $k_{Bend}/(k_BT/b_0)$	200
Varied grid size a_{grid}/b_0	19, 18, 17, 16, 15, 14, 13, 12
Corresponding α	1.07, 1.01, 0.95, 0.89, 0.83, 0.77, 0.71, 0.65

Table 3.3: Parameters used to investigate the influence of the pore size on the cell behaviour.

Introduced parameter	Definition
Mean cell speed v_z^*	The time it took the cell's center of mass to travel from the beginning to the end of the network was averaged over the ensemble.
Speed enhancement Δv_z^*	The maximum value of the pore-averaged speed curve was taken, then the terminal velocity was subtracted, and the resulting value was ensemble-averaged.
Total energy at speed maximum $E^*_{Tot,v_{peak}}$	Both speed and total energy curves were pore-averaged. The total energy was evaluated at the time of the speed maximum and then ensemble-averaged.
Maximum bending energy $E^*_{Bend,max}$	The maximum bending energy value of the pore-averaged curve was taken and averaged over the ensemble.

Table 3.4: Definition of introduced properties.

The top plot in figure 3.9 shows the mean cell speeds in units of the corresponding terminal velocity as a function of the bending elasticity k_{Bend}. The measured ensemble means are plotted including error bars. One can see that starting at $k_{Bend} = 0$ the mean cell speed has a value of about 0.816, with the mean cell speed increasing for increasing k_{Bend}. The slope then flattens and seems to reach a maximum mean cell speed of about 0.833 between $k_{Bend} = 85$ and $k_{Bend} = 90$. After the peak, the mean cell speed decreases for increasing k_{Bend} down to a speed of about 0.823 for $k_{Bend} = 200$. The bottom plot in figure 3.9 shows the speed enhancement Δv_z^* after each pore, plotted as a percentage measure. This parameter seems to grow monotonously with increasing k_{Bend}, from an enhancement of about 2% at $k_{Bend} = 0$ to about 10 % at $k_{Bend} = 200$. The curve seems to flatten slightly towards larger k_{Bend}.

Figure 3.10 shows the same types of plots as a function of pore size α. The top plot, however, now has a reversed x-axis, such that the pore size decreases going to the right. As expected, the mean cell speed is unaffected by the network for $\alpha > 1$, such that the cell speed is equal to the terminal velocity in a network-free fluid. With decreasing α, the mean cell speed decreases, with the slope of the curve getting steeper as α decreases. The smallest simulated pore size of about 0.65 results in a mean migration speed of about 0.82. The bottom plot in figure 3.10 shows the speed enhancement Δv_z^* after each pore as a function of pore size. This value increases for decreasing α, with the slope also getting steeper as α decreases. Comparing both figures 3.9 and 3.10 shows the similarities as well as the differences of the influence of both bending elasticity and pore size. While the pore size size has a monotonous effect on the mean cell speed, varying the bending elasticity leads to a unimodal behaviour. It is also apparent that varying the pore size leads to larger variations in cell speed than varying the bending elasticity. A larger speed enhancement, however, is obtained by either increasing bending elasticity or decreasing the pore size. The fact that the speed enhancement is larger than zero for $\alpha > 1$ can be reduced to the fact that its value was determined using the maximum local speed value, which is affected by thermal noise for small values.

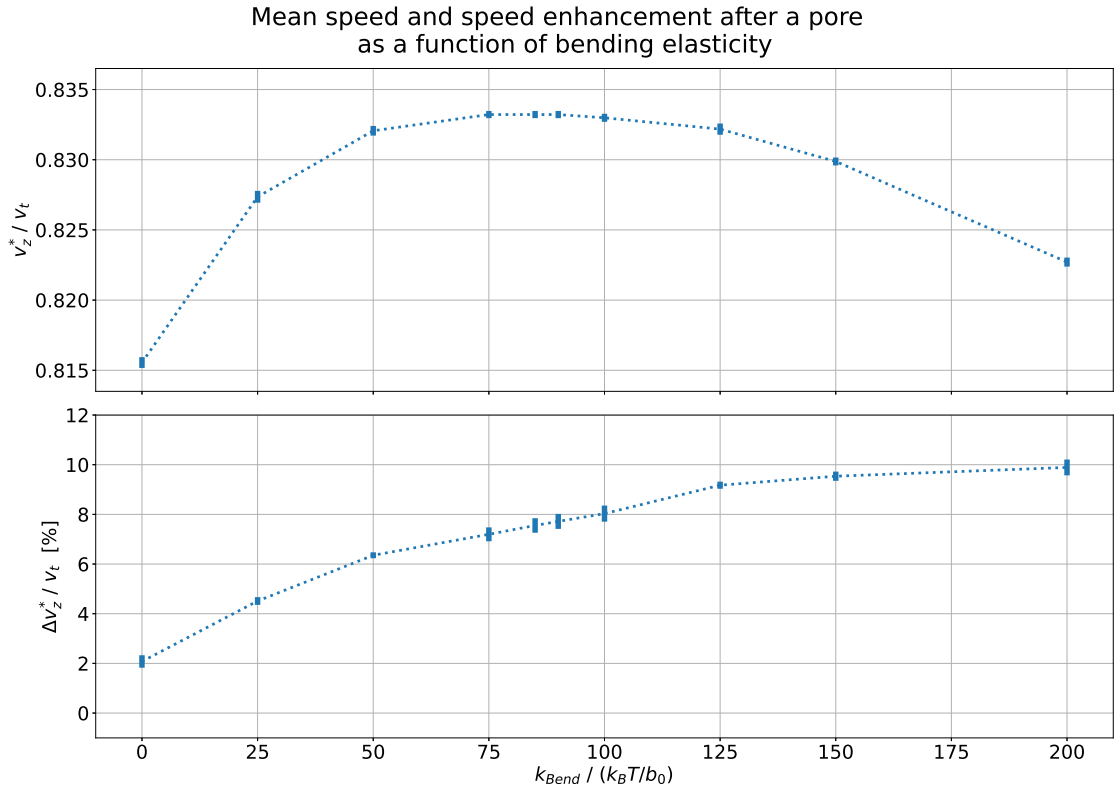

Figure 3.9: Influence of bending elasticity on mean cell speed and speed enhancement after each pore.

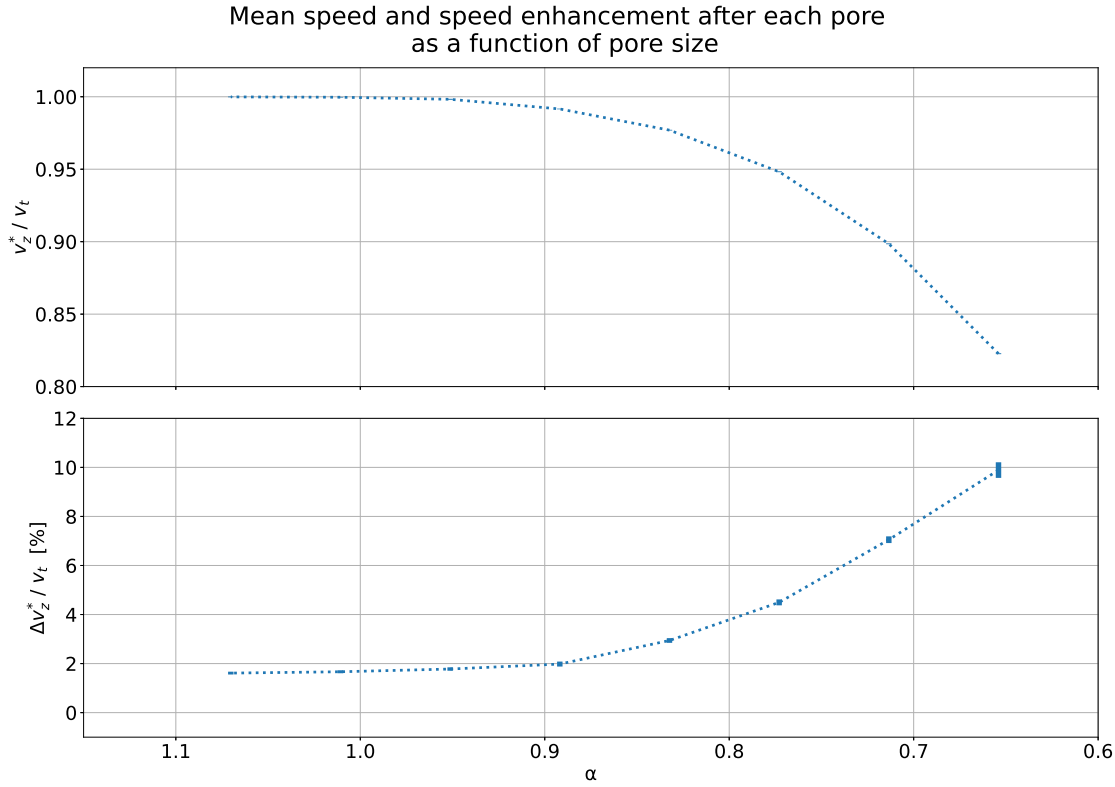

Figure 3.10: Influence of bending elasticity on mean cell speed and speed enhancement after each pore.

Correlations of cell speed properties and interaction energies

In order to explain the trends observed in figures 3.10 and 3.9, some parameter correlations were investigated. The speed enhancement was observed to show similar behaviour as the mean maximum value of the total interaction energy at the point in time of the speed maximum, denoted in the plots as $E^*_{Tot,v_{peak}}$. This correlation is shown as a function of bending elasticity in figure 3.11 and as a function of pore size in figure 3.12.
These correlations motivate the interpretation that elastic energy created by the surface deformations is utilized to locally enhance the cell speed after the pores. Since surface deformations not only lead to a change of total curvature, but also potentially to a change in bond lengths, volume, and surface area, all of the cell interaction potentials contribute to this elastic energy, not just the bending potential. This explains the large correlation of the speed enhancement with the total interaction energy at the same time. The bending energy alone at that point in time was found to show a less convincing correlation with the observed curve of the speed enhancement.
The unimodal behaviour of the mean cell speed as a function of the bending elasticity k_{Bend} is an unexpected finding. The parameter k_{Bend} represents the interaction strength of the cell surface bending potential. Its corresponding minimum energy configuration is a flat sheet. Therefore, a larger k_{Bend} corresponds to a surface which has a stronger desire to reduce its total curvature, which means that surface deformations cost more energy. So, starting from a configuration that can squeeze through the network, the naive assumption would be that increasing k_{Bend} leads to a stronger resistance to surface deformations and thus to a lower mean cell speed. Further increasing k_{Bend} could then lead to a discrete hopping regime, and eventually to the cell getting stuck in a pore. This would motivate the right part of the unimodal curve, but fails to explain

the left part.

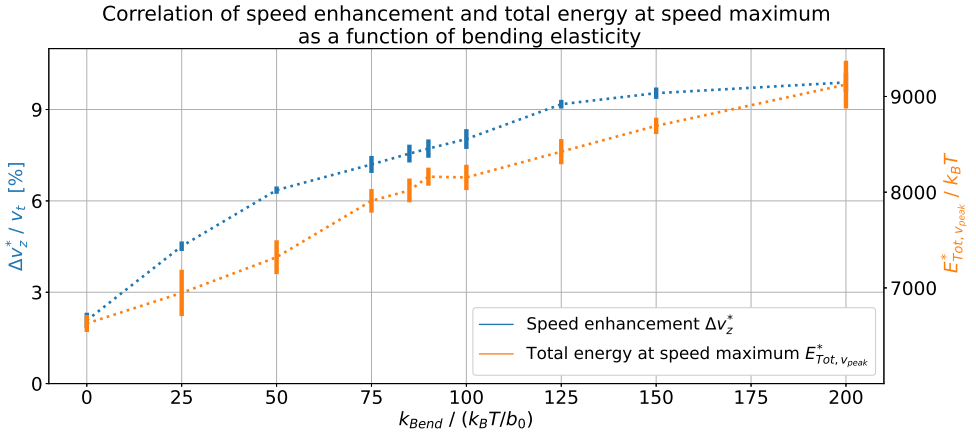

Figure 3.11: Correlation of speed enhancement and total energy at the speed maximum as a function of bending elasticity.

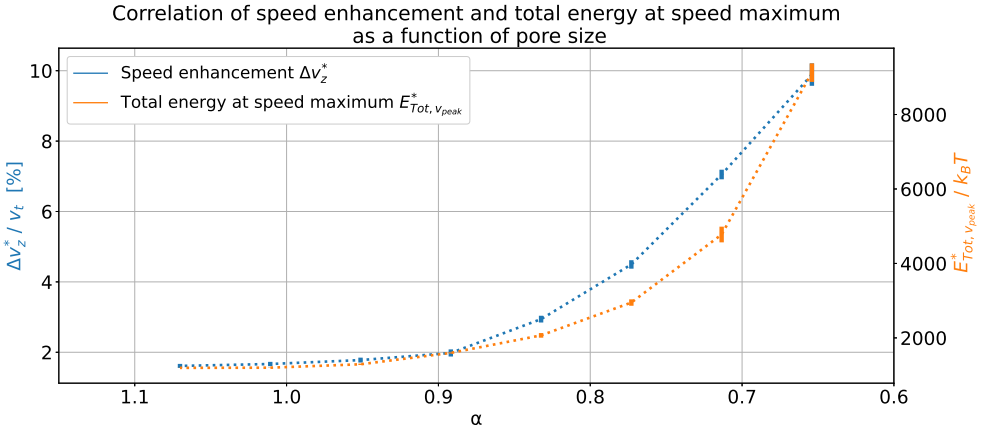

Figure 3.12: Correlation of speed enhancement and total energy at the speed maximum as a function of pore size.

Figures 3.13 and 3.14 show a comparison of the behaviour of the mean cell speed and the maximum bending energy $E^*_{Bend,max}$. Interestingly, the mean maximum bending energy shows both the monotonous behaviour of the mean cell speed as a function of pore size as well as the unimodal behaviour of the mean cell speed as a function of bending elasticity. The curves of the mean cell speed and the maximum bending energy show similar behaviour in general, but also deviations at a closer look. The peak value as a function of bending elasticity is achieved at a larger value of k_{Bend} and the curve seems to fall quicker as a function of pore size. This implies that the maximum bending energy is related to the mean cell speed, but does not define it alone. Due to the observed correlations of maximum bending energy and mean cell speed, a possible interpretation for the left part of the unimodal behaviour would be that including a bending potential could lead to local flattening of the cell surface near the interaction sites with the network. This flattening could in principle lead to weaker cell-network interactions such that the pore acts as a weaker barrier, facilitating the cell propagation, such that the mean speed could increase with k_{Bend} for small values of k_{Bend}. However, the WCA energy representing the cell-network interactions was found to follow a monotonous curve as a function of bending elasticity. Therefore, this interpretation does not seem to agree with the simulation results.

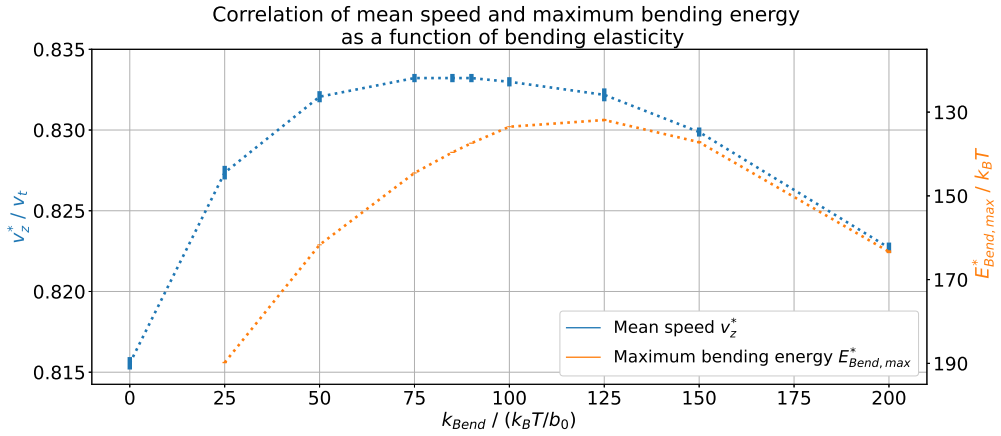

Figure 3.13: Correlation of mean cell speed and maximum bending energy as a function of bending elasticity.

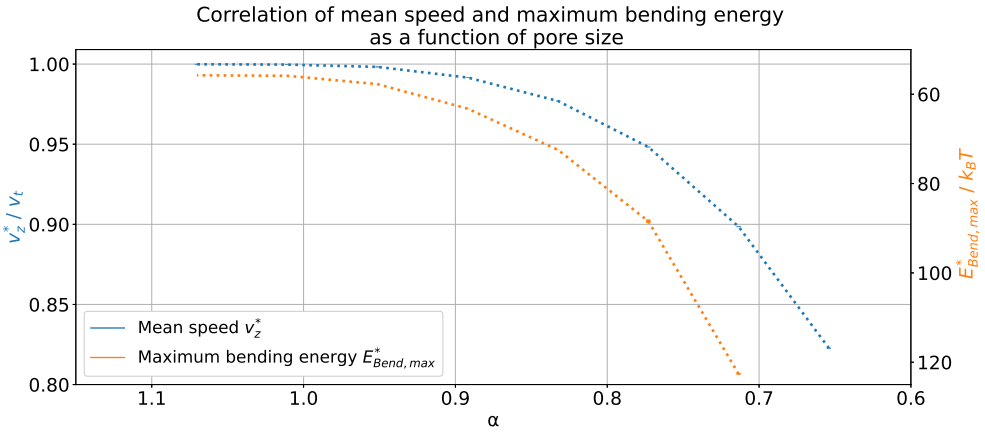

Figure 3.14: Correlation of mean cell speed and maximum bending energy as a function of pore size.

3.3 Driven deformable cells in deformable networks

Deformable network models

In order to investigate the general case of a driven deformable cell in an ordered deformable network, simulations were also run using a non-rigid network. Since in this case boundary effects play a role, the network size along the x- and y-direction was increased from $N_{cells,xy} = 1$ (a single channel) to $N_{cells,xy} = 5$. The network size along the z-direction was not changed at $N_{cells,z} = 10$. The deformability of the network was modelled by including a polymer bending potential, an attractive FENE potential as well as a repulsive WCA potential within the individual polymer chains of the network. The interaction parameters for the polymer network were based on the polymer model by Kremer and Grest [25]. The FENE parameters were thus chosen to be $k_{FENE} = 30$ and $\Delta r_{max} = 1.5$, while the WCA parameters were chosen to be $\epsilon = \sigma = 1$.

Simulations of the network alone were performed to estimate the network's equilibration time.

k_{FENE} / (k_BT/b_0^2)	30
Δr_{max} / b_0	1.5
ϵ / k_BT	1
σ / b_0	1
$k_{Bend,NW}$ / k_BT	100
$a_{grid,initial}$ / b_0	11

Table 3.5: Network parameters used to estimate equilibration time.

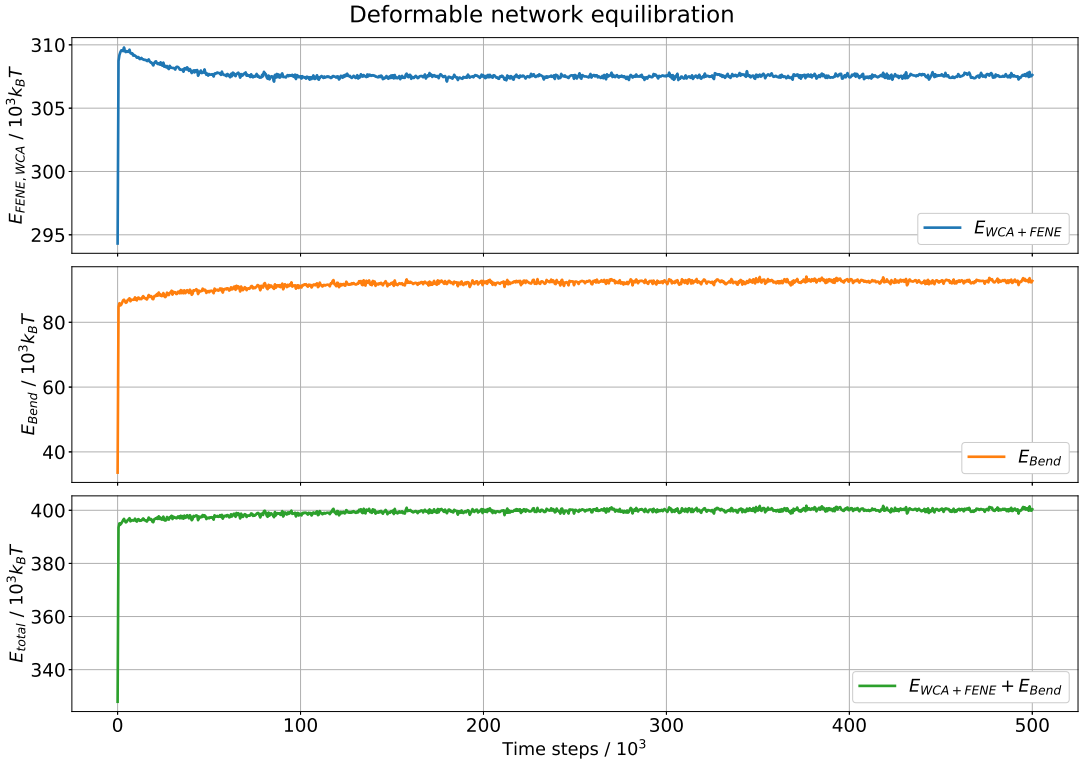

Figure 3.15: Time evolution of the energy contributions of an equilibrating deformable network. The upper two plots show the individual contributions from the WCA+FENE and the bending potential, respectively, while the bottom plot shows the total energy as a function of time.

The simulations were attempted using different choices of boundary conditions like freely equilibrating boundary nodes or initializing the boundary nodes as damped rigid walls. However, this revealed that the implemented network remained stable only for rather weak polymer chain bending potentials. Instability in this case refers to some polymer chain bonds acquiring a bond length near or larger than the maximum bond length of the respective FENE potential, such that the bond interaction essentially vanishes, potentially leading to large repulsive force and neighbouring bonds becoming unstable. Deviating from the Kremer-Grest parameter choice did not seem to improve the stability. This already restricted the range of possible values for the network bending elasticity $k_{Bend,NW}$. A stable network equilibration was achieved for the network parameters described in table 3.5. The initial grid size was chosen to be $a_{grid,initial} = 11$. It should be noted though that the physical pore size of the equilibrated network can deviate from this initial value.

Figure 3.15 shows the energy evolution of a single simulation of a deformable network simulated for $5 \cdot 10^5$ time steps. Measurements were taken every 500 time steps. The boundary beads were fixed at the simulation box walls from the start of the simulation. The used interaction parameters are summarized in table 3.5. The plots show that, due to the choice of interaction parameters, the bond energies (WCA+FENE) have a larger energy contribution than the network bending energies. While the bond energies peak at the start and then decrease, the bending energies increase monotonously, until both energy curves approach a plateau value after an equilibration time of approximately $2.5 \cdot 10^5$ time steps.
The Visualization in figure 3.16 shows a comparison of the initialized network configuration (red) and equilibrated network configuration (blue). Looking at the vertical boundary chains on the left and right end of the network, one can see that, during equilibration, the network tries to contract due to entropic reasons. This means that the equilibrated network is under tension due to the choice of boundary conditions. As a result, the effective grid size $a_{grid,eff.}$ in the center of the network is smaller than the initial value of $a_{grid,initial} = 11$. This is also visible in figure 3.16.

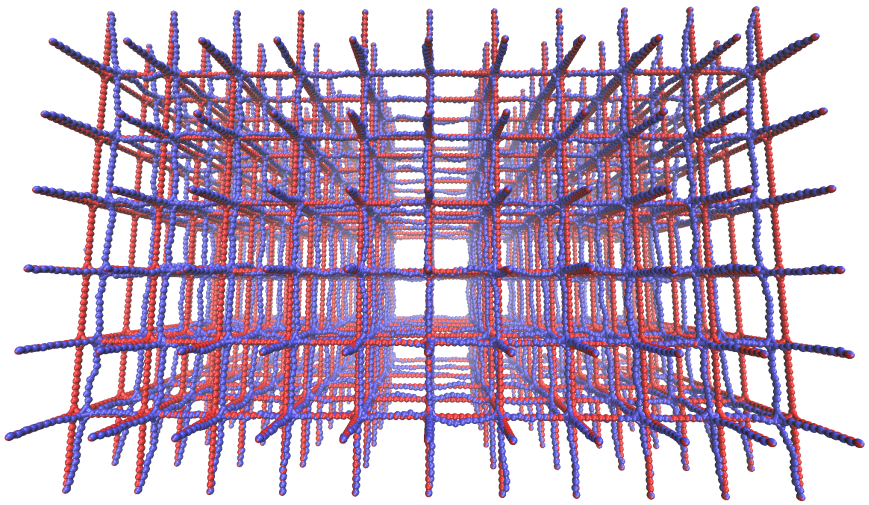

Figure 3.16: Visualization of the equilibration of a deformable network. The blue beads represent the initialized network configuration, while the red beads represent the equilibrated network configuration.

Driven deformable cells in deformable networks

Attempts to simulate a rigid cell being pulled through a deformable network were found to be stable as long as the grid size *a* is larger than, equal to, or only slightly smaller than the cell diameter $2R_{cell}$. Trying to choose a smaller a_{grid} in order to reproduce a rigid cell attempting to translocate through a pore and getting stuck resulted in an unstable network. Similar behaviour was found for deformable cells in deformable networks. For sufficiently small a_{grid}, depending on the chosen interaction parameters, either the cell or the network become unstable before the cell can pass the first network pore. In the case of the cell, instability means that some bond lengths diverge leading to a ruptured cell surface.
A stable example run was performed using a network with the network parameters described in table 3.5 and a driven deformable cell with the same parameters as in the discussion of the generic behaviour of deformable cells in rigid networks (table 3.1). Figure 3.17 shows different properties of the system's behaviour over time.

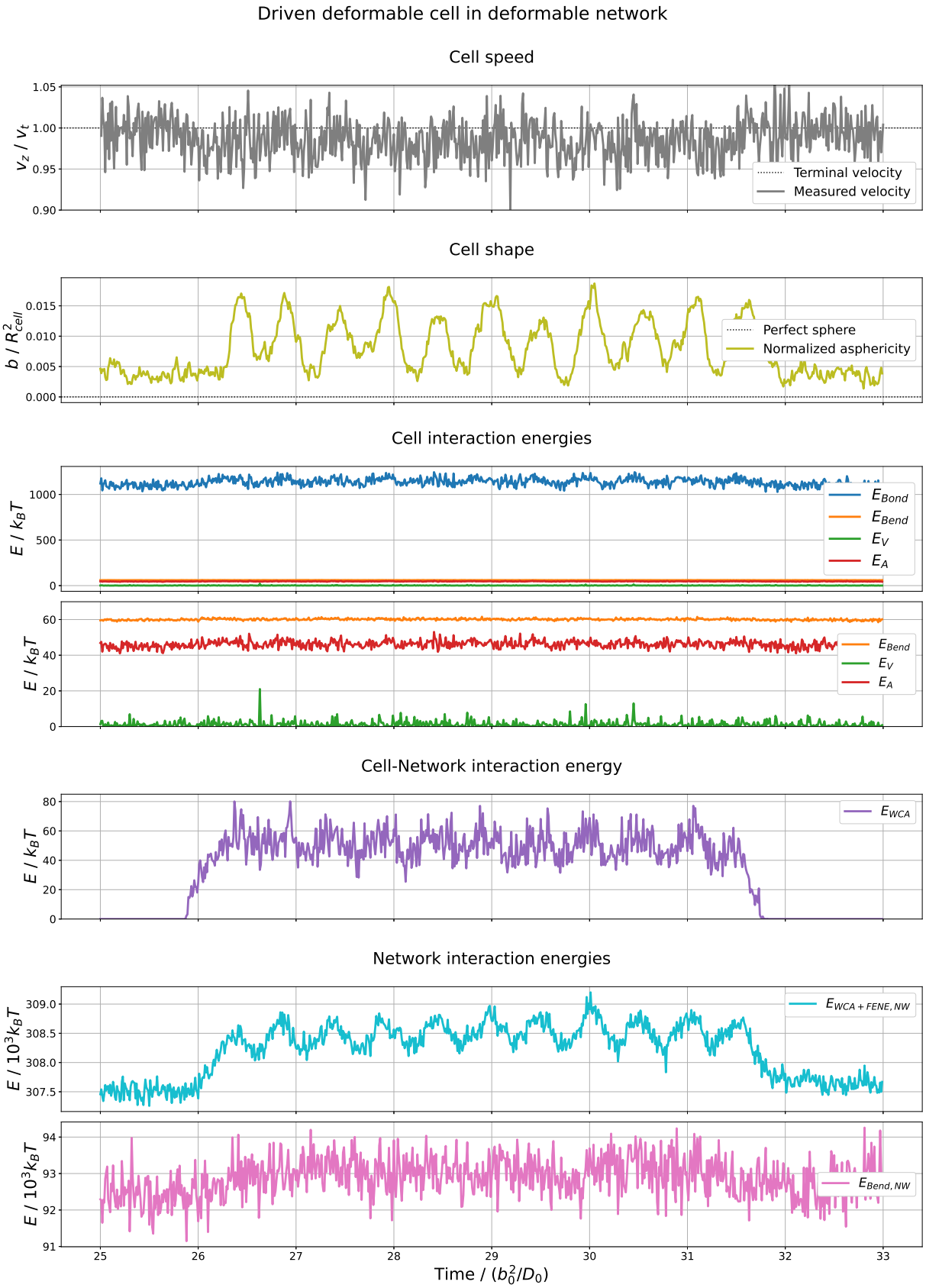

Figure 3.17: Time evolution of driven deformable cell in deformable network.

The shown plots skip the equilibration time of the network of about 25 $\frac{b_0^2}{D_0}$. Measurements were taken every 100 time steps. The cell speed shows very weak oscillatory behaviour with the expected speed drops when encountering a pore. The general speed evolution, however, is strongly influenced by thermal fluctuations. The cell shape represented by the normalized asphericity shows a more pronounced oscillatory behaviour. The oscillation amplitude is rather small though, with a peak value of about 0.017. This is about a tenth of the value observed in the rigid network case in figure 3.7. One can see that the maximum value in each oscillation period varies more strongly than in the case of the rigid network. This can be explained by the fact that the network now also reacts to cell-network interactions with deformations. This means that the cell encounters each pore in a different configuration, due to previous cell-network interactions as well as thermal fluctuations. The cell interaction energies are dominated by thermal fluctuations and do not show clear oscillatory behaviour. The point of first contact of cell and network can be seen as a steep increase in the WCA energy representing the cell-network interaction. This curve also shows week oscillatory behaviour as long as the cell travels inside the network. The network bond energies (WCA+FENE) show clear oscillatory behaviour, while the network bending energy is dominated by thermal fluctuations. Figure 3.18 shows a visualization of this simulation. Comparing snapshots 2 and 4, one can see at the example of the upper network chain of the first pore how the network deforms, enabling the cell to swim through the pore. Due to the choice of parameters this is more like a sliding than a squeezing motion. Very weak deviations of the cell surface from the spherical shape are visible, while change in the network configuration is more dominant. This behaviour can be traced back to the rather weak network bending potential (small $k_{Bend,NW}$). In order to reproduce squeezing behaviour in a deformable network, adjustments to the model would need to be made in order to prevent instabilities.
This simulation using a deformable network was performed as a proof of concept for the implementation of the deformable network model. However, the discussed instabilities made it difficult to reproduce the desired squeezing behaviour of the cell. A smaller grid size as well as a stronger network bending potential are necessary to reproduce squeezing behaviour.

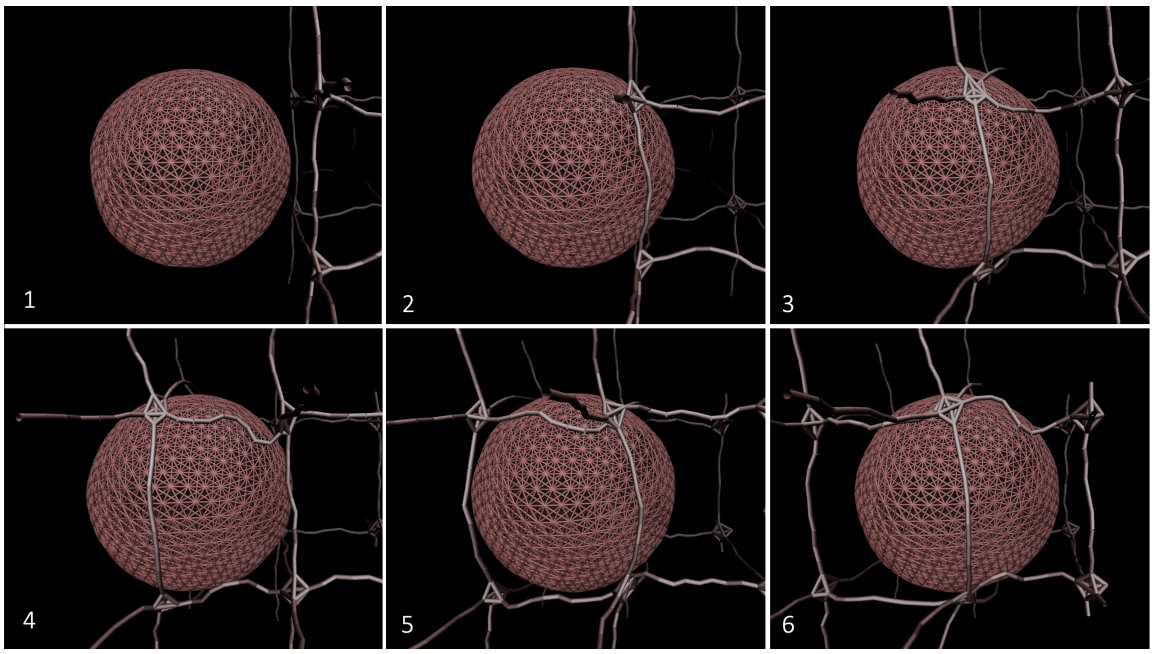

Figure 3.18: Visualization of a deformable cell in a rigid network.

Chapter 4

Conclusion

This project studied the influence of pores in biopolymer networks such as the ECM on the speed and surface deformation of cells, using a simplified model of an externally driven deformable cell moving through ordered polymer networks by means of Brownian dynamics simulations.
A driven deformable cell moving through a rigid network was used to investigate and discuss the generic cell surface behaviour when squeezing through a pore. The cell speed was shown to have oscillatory behaviour with speed minima before and subsequent maxima after each pore. The speed maxima were larger than the respective terminal velocities in a network-free fluid. All energy contributions showed oscillatory behaviour with small phase shifts between the different types of contributions. In order to squeeze through the pores, the cell surface needs to deform. This was visible in the time evolution of the cell asphericity with periodic changes to a more elliptical surface shape.
Simulations for different bending elasticities and pore sizes revealed different effects. The speed enhancement increased monotonously both with increasing bending elasticity and decreasing pore size. Taking into account the strong correlations between the speed enhancement and the total cell interaction energy at the speed maximum, this indicates that during the squeezing process the cell utilizes elastic energy from the surface deformations in order to locally enhance its speed. The mean cell speed showed a monotonous curve as a function of pore size, but a unimodal behaviour as a function of bending elasticity. Both trends are mirrored by the maximum bending energy, implying a causal relationship between the two properties. These observations invite further research to investigate how the interplay of cell and cell-network interactions gives rise to this unimodal behaviour.
In addition, simulations using a deformable network were performed successfully, showing oscillatory behaviour in some cell and network properties which represents the bi-directional mechanical crosstalk of cell and network. For stability reasons, a weak network bending potential as well as a rather large pore size were used. Therefore, the cell did not need to squeeze considerably. Although some properties like the cell speed and shape or the network bond interaction energy revealed clear oscillatory behaviour, the cell-network interactions were not strong enough to generate significant deformations which could lead to a significant local speed enhancement after the pores. Still, the mean cell speed showed slight periodic drops.

It should be noted that even with $k_{Bend} = 0$, the cell surface resists bending while squeezing through the pore due to the presence of further interaction potentials. This means that the phys-

ical bending elasticity of the cell surface is not defined by k_{Bend} alone, but by the combination of all cell surface interactions. In order to investigate the contributions of the different potentials one could perform simulations with varying interaction strengths for each cell surface interaction potential.
In the course of this project, simulations were performed for different bending elasticities and pore size with one of those fixed while the other is varied, respectively. Instead of obtaining just two single curves, one could perform such simulations using a parameter grid of different combinations of bending elasticity and pore size. This could give a clearer image of how the interplay of cell bending elasticity and pore size determines properties like the cell speed.
In order to understand the interplay of cell elasticity and network elasticity, further detailed simulations using a deformable network are necessary. The observed instabilities of the cell surface could potentially be avoided by including Stillinger-Weber (SW) potentials. However, the different SW interaction parameters would have to be finely tuned such that the SW potentials do not themselves contribute to instabilities. The network bond instabilities were accompanied by network bonds acquiring bond lengths near or larger than the FENE maximum bond length Δr_{max}. In principle, one could attempt to resolve this issue by changing the FENE interactions parameters. A few first attempts to do so were unsuccessful in the course of this project. Alternatively, the instabilities could be prevented by choosing a different type of potential to simulate the attractive interactions of network beads. In both cases, it may be helpful to have a closer look at the time evolution of the network bond length distribution and use this insight to change the different interaction parameters.
In biological cells, the properties of the cell nucleus are a major factor limiting the migration speed when squeezing through pores [8]. This has to be taken into account when building a realistic cell model. As an addition to the model used in this project, one could add a second triangulated surface within the cell surface. By using a different interaction strength, this could be a simple model of the cell's nucleus. This way, when squeezing through a pore, the cell's outer surface has to deform first. However, at a certain point, when the pore size gets smaller than the nucleus size, the nucleus surface has to deform as well. Results from such simulations could then be compared to measurements from experiments.

In conclusion, this simulation study has shown that the pore size and bending elasticity have different effects on the cell speed of a driven cell in an ordered rigid polymer network. While the cell speed as a function of pore size shows monotonous behaviour, the cell speed as a function of bending elasticity shows a unimodal curve. After having squeezed through a pore, the simulated cells showed a local speed enhancement, which grows with both a decreasing pore size and larger bending interaction strength. In order to fully explain this phenomenona, further research is needed. Further simulations using deformable networks are also needed to investigate the general cell behaviour in a more realistic environment.

Bibliography

[1] Kameritsch, P., Renkawitz, J. (2020). Principles of Leukocyte Migration Strategies. Trends in cell biology, 30(10), 818–832. https://doi.org/10.1016/j.tcb.2020.06.007

[2] Yamada KM, Sixt M. Mechanisms of 3D cell migration. Nat Rev Mol Cell Biol. 2019 Dec;20(12):738-752. doi: 10.1038/s41580-019-0172-9. Epub 2019 Oct 3. PMID: 31582855.

[3] Nakamura S, Minamino T. Flagella-Driven Motility of Bacteria. Biomolecules. 2019 Jul 14;9(7):279. doi: 10.3390/biom9070279. PMID: 31337100; PMCID: PMC6680979.

[4] Man Y, Ling F, Kanso E. Cilia oscillations. Philos Trans R Soc Lond B Biol Sci. 2020 Feb 17;375(1792):20190157. doi: 10.1098/rstb.2019.0157. Epub 2019 Dec 30. PMID: 31884917; PMCID: PMC7017329.

[5] Charras, G., Sahai, E. Physical influences of the extracellular environment on cell migration. Nat Rev Mol Cell Biol 15, 813–824 (2014). https://doi.org/10.1038/nrm3897

[6] Wirtz, D., Konstantopoulos, K. & Searson, P. The physics of cancer: the role of physical interactions and mechanical forces in metastasis. Nat Rev Cancer 11, 512–522 (2011). https://doi.org/10.1038/nrc3080

[7] van Helvert, S., Storm, C. & Friedl, P. (2018). Mechanoreciprocity in cell migration. Nat Cell Biol 20, 8–20. https://doi.org/10.1038/s41556-017-0012-0

[8] McGregor, A. L., Hsia, C. R., & Lammerding, J. (2016). Squish and squeeze-the nucleus as a physical barrier during migration in confined environments. Current opinion in cell biology, 40, 32–40. https://doi.org/10.1016/j.ceb.2016.01.011

[9] Paul CD, Mistriotis P, Konstantopoulos K. Cancer cell motility: lessons from migration in confined spaces. Nat Rev Cancer. 2017 Feb;17(2):131-140. doi: 10.1038/nrc.2016.123. Epub 2016 Dec 2. PMID: 27909339; PMCID: PMC5364498.

[10] Peltomäki, M. & Gompper, G. (2013). Sedimentation of single red blood cells. Soft Matter. 9. 8346. 10.1039/c3sm50592h.

[11] Noguchi H., Gompper G., Shape transitions of fluid vesicles and red blood cells in capillary flows, Proc. Natl. Acad. Sci. USA 102 (2005) 14159–14164.

[12] Guckenberger A, Gekle S. Theory and algorithms to compute Helfrich bending forces: a review. J Phys Condens Matter. 2017 May 24;29(20):203001. doi: 10.1088/1361-648X/aa6313. Epub 2017 Feb 27. PMID: 28240220.

[13] Guckenberger, A., Schraml, M. P., Chen, P.G., Leonetti, M., & Gekle, S. (2016). On the bending algorithms for soft objects in flows. Computer Physics Communications, 207, 1-23. https://doi.org/10.1016/j.cpc.2016.04.018.

[14] Campbell EJ, and Bagchi P. A Computational Model of Amoeboid Cell Swimming. Phys Fluids (2017) 29:101902. doi:10.1063/1.4990543

[15] Campbell EJ, Bagchi P. A computational model of amoeboid cell motility in the presence of obstacles. Soft Matter. (2018) 14:5741–63. doi: 10.1039/C8SM00457A

[16] Software: Visual Molecular Dynamics (VMD). https://www.ks.uiuc.edu/Research/vmd/

[17] Brańka, A. C., & Heyes, D. M. (1999). Algorithms for Brownian dynamics computer simulations: multivariable case. Physical review. E, Statistical physics, plasmas, fluids, and related interdisciplinary topics, 60(2 Pt B), 2381–2387. https://doi.org/10.1103/physreve.60.2381

[18] Huber, G. A., & McCammon, J. A. (2019). Brownian Dynamics Simulations of Biological Molecules. Trends in chemistry, 1(8), 727–738. https://doi.org/10.1016/j.trechm.2019.07.008

[19] Marsaglia, G., & Tsang, W. W. (2000). The Ziggurat Method for Generating Random Variables. Journal of Statistical Software, 5(8), 1–7. https://doi.org/10.18637/jss.v005.i08

[20] Dinas, S. & Bañón, J. (2014). A REVIEW ON DELAUNAY TRIANGULATION WITH APPLICATION ON COMPUTER VISION. IJCSE - International Journal of Computer Science and Engineering. 3. 9-18.

[21] Lee, D.T., Schachter, B.J. (1980). Two Algorithms for Constructing a Delaunay Triangulation. International Journal of Computer and Information Sciences, Vol. 9, No. 3

[22] Seifert, U. (1997) Configurations of fluid membranes and vesicles, Advances in Physics, 46:1, 13-137, DOI: 10.1080/00018739700101488

[23] Grest, G.S. & Kremer,K. (1990). Macromolecules. 23 (23), 4994-5000. DOI: 10.1021/ma00225a020

[24] J. D. Weeks, D. Chandler, and H. C. Andersen, J. Chem. Phys. 54, 5237 1971.

[25] Grest GS, Kremer K. Molecular dynamics simulation for polymers in the presence of a heat bath. Phys Rev A Gen Phys. 1986 May;33(5):3628-3631. doi: 10.1103/physreva.33.3628. PMID: 9897103.

[26] Allen, M., & Tildesley, D. (2017-06-22). Computer Simulation of Liquids: Second Edition. : Oxford University Press. Retrieved 20 Jun. 2022, from https://oxford.universitypressscholarship.com/view/10.1093/oso/9780198803195.001.0001/oso-9780198803195.

Attachments

Zusammenfassung

Zellen migrieren in verschiedenen Umgebungen und als Reaktion auf verschiedene Einflüsse. Ein Beispiel von Zellmigration ist die Bewegung von Leukozyten durch komplexe Umgebungen, in denen sie unter anderem kleine Poren in der Extrazellulären Matrix (EZM) durchdringen, indem sie ihre Zellmembran erheblich deformieren müssen. [1]
Das Ziel dieses Projekts war es, die Auswirkungen von Poren auf die Geschwindigkeit und Oberflächenverformungen von Zellen zu untersuchen. Dies geschah unter Benutzung eines vereinfachten Modells einer extern angetriebenen Zelle in einem geordneten Polymernetzwerk.
Zelle und Netzwerk wurden dabei modelliert als Strukturen aus diskreten Teilchen, welche über bestimmte Interaktionspotentiale in einer thermischen Umgebung miteinander wechselwirken. Eine extern angelegte Kraft wurde benutzt, um die Fortbewegung der deformierbaren Zelle im Netzwerk mithilfe der Simulationsmethode der Brownschen Dynamik zu untersuchen.
Ein starres Polymernetzwerk wurde als erstes vereinfachtes Modell von Poren im EZM verwendet. Die resultierende Geschwindigkeit der angetriebenen Zelle zeigt oszillierendes Verhalten mit Minima vor und Maxima nach Durchdringen der jeweiligen Netzwerk-Pore. Die Geschwindigkeits-Maxima können die Endgeschwindigkeiten der jeweiligen Zelle in der netzwerk-freien Flüssigkeit überschreiten, während der Wert des Geschwindigkeits-Maximums mit der gesamten Interaktionsenergie der Zelle am selben Zeitpunkt zusammenhängt. Dies weist darauf hin, dass während des Deformierens elastische Interaktionsenergie verwendet wird um die Zellgeschwindigkeit lokal zu steigern. Die mittlere Zellgeschwindigkeit durch das Netzwerk zeigt ein nicht-lineares unimodales Verhalten als Funktion der Biegesteifigkeit. Dieser unimodale Verlauf zeigt sich ebenfalls in der maximalen Biegeenergie, was einen kausalen Zusammenhang zwischen diesen beiden Parametern nahelegt.
Zuletzt wurden Simulationen mit einem deformierbaren Netzwerk erfolgreich durchgeführt, welche oszillierendes Verhalten von Zell- und Netzwerk-Eigenschaften zeigen. Dies zeigt die gegenseitige Beeinflussung von Zelle und Netzwerk.